Cosmological radiative transfer at the epoch of reionization

Master's Thesis
Institute for Theoretical Physics
University of Zürich

Timothy Stranex
Supervisor: Prof. Dr. Romain Teyssier

Abstract

The epoch of reionization is thought to be driven by ionizing radiation from galaxy and quasar sources. Numerical simulations of this require solving for radiative transfer in addition to gas hydrodynamics and gravity in an expanding universe. We create a code suitable for these simulations by combining RAMSES[19], a hydrodynamics code, with ATON[1], a radiative transfer code. The new code produces results comparable to other radiative transfer codes on standard test cases. We also run a small cosmological simulation and obtain results that qualitatively reproduce the epoch of reionization. A self-shielding effect is observed in which the radiation is unable to penetrate into very dense gas clumps. Finally, future applications for the code are discussed.

Zürich, December 2010

Contents

1   Introduction

In the standard models of cosmology, the universe was initially extremely small, dense and hot about 13.7×10^9 years ago [7]. It then began expanding under the action of gravity. The expansion caused it to gradually cool and become less dense. Tiny fluctuations in the early conditions were reinforced by gravity and grew to become the galaxies and quasars we see today. Fig. 1 is a diagram of this process.

The universe in its extreme early form is best described as a sea of interacting particles in thermal equilibrium. But as the universe expanded, various types of particle began to drop out of equilibrium. In particular, around redshift $z = 1100$, the electrons and protons recombined to form neutral hydrogen thus becoming decoupled from the photons. The photons were then left mostly undisturbed until today where we observe them as $2.73\,\mathrm{K}$ blackbody radiation in the **cosmic microwave background** (CMB). The CMB is extremely useful in that it gives us a detailed picture of the universe at this early time. The WMAP satellite was built to observe the CMB. The data it collects is used to precisely determine the parameters of cosmological models [15]. We will use these parameters to generate the initial conditions of our simulations.

The CMB contains tiny variations over the sky. As the universe aged, the corresponding matter pertrubations from this early time grew because gravity tends to pull the overdensities together. These variations can be understood using perturbation theory while they are small but eventually they grow large enough that a nonlinear treatment is needed. This is best done using numerical techniques.

The universe consists of roughly 16% "baryonic" matter (protons and electrons) and 84% dark matter. Dark matter is collisionless and interacts only through gravity. It is usually simulated using n-body particle codes. It is usually sufficient to use Newtonian gravity (with an expanding background). Baryonic matter can be modelled as a gravitationally-influenced fluid. This requires a hydrodynamics solver [6]. There are several codes which implement these two techniques. We will be using the RAMSES code [19]. In these nonlinear simulations, we find that some perturbations collapse into very dense objects. Stars form inside these dense objects and they become galaxies.

After recombination, the gas in the universe is mostly neutral. However, we observe today that that intergalactic medium is highly ionized [20] and has been so since at least redshift $z_{\mathrm{reion}} \approx 6$. So between recombination and z_{reion}, some process must have ionized the universe. This process is called **reionization**. Reionization is thought to be caused by the emission of ultra-violet radiation from early galaxies and quasars. These UV photons have enough energy to ionize neutral hydrogen. See [4] for a review of the history of the intergalactic medium.

Reionization is a complicated process. There are no detailed analytical models and much of the process has to be understood through simulations. Reionization is seen to proceed by the growth of bubbles of ionized gas around the radiation sources. These bubble expand and merge with others until eventually they fill the entire universe and reionization is complete. In order to simulate reionization, it is necessary to include the effects of radiative transfer in the standard cosmological n-body and hydrodynamics codes. See [20] for a review of reionization simulations.

The speed of light is usually orders of magnitude higher than the speed of sound in the gas. This makes radiative transfer very computationally intensive because the time step must be very small. Another difficulty is the high range of space and mass resolution required. To track the radiation in detail around the galactic sources, a resolution of at least $10\,\mathrm{kpc}$ is required. On the other hand, the box size should be at least $100\,\mathrm{Mpc}$ to obtain a representative distribution of galaxies. The large size is also needed because the mean free path of photons can reach $10\,\mathrm{Mpc}$.

In this project, we will develop a code for simulating reionization. We will use RAMSES for n-body gravity and hydrodynamics and ATON [1] for radiative transfer. Previously these two codes have been used together by post processing the RAMSES results with ATON to obtain the radiation field [2]. This is not ideal because the radiation is unable to influence the hydrodynamics. The new code will couple the radiation and hydrodynamics solvers together so that they can influence each other directly.
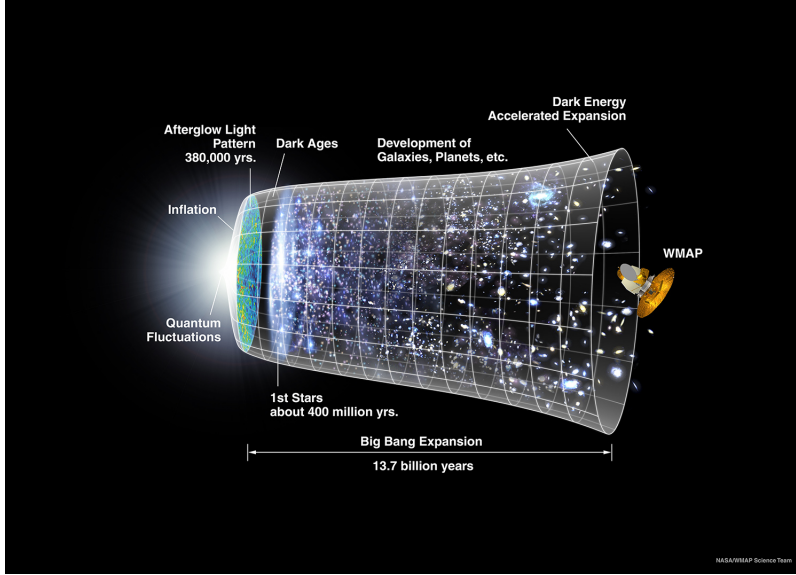
Figure 1: The history of the universe. Credit: NASA / WMAP Science Team

2 The model

Cosmology is based on many physical processes. For our purposes of simulating structure formation and reionization, we need to include gravity, gas hydrodynamics, chemistry, cooling, and radiative transfer. This section describes the basic equations that must be solved. See [6] for more details on the methodology of hydrodynamic simulations for cosmology.

2.1 Gravity and dark matter

Newtonian gravity is governed by

$$\nabla^2 \phi = 4\pi G(\rho_{\text{total}} - \rho_{\text{total,background}}) \tag{1}$$

where ρ_{total} is the total mass density including the gas, dark matter and stars.

Unlike the gas, dark matter is collisionless and the dark matter particles move under the force of gravity only. The position and velocity of a dark matter particle evolves according to

$$
\begin{aligned}
\frac{d\mathbf{x}}{dt} &= \mathbf{v}, \\
\frac{d\mathbf{v}}{dt} &= -\nabla\phi.
\end{aligned}
\tag{2}
$$

2.2 Hydrodynamics

The interstellar gas is assumed to be highly collisional and in local thermal equilibrium. As such, the gas particles have a Maxwell-Boltzmann distribution and the gas has no viscosity or heat conduction. Therefore,

the gas can be described by the Euler fluid equations. The Euler equations in their conservative form are:

$$\frac{\partial \rho}{\partial t} + \nabla \cdot (\rho \mathbf{u}) = 0,$$

$$\frac{\partial (\rho \mathbf{u})}{\partial t} + \nabla \cdot (\rho \mathbf{u} \otimes \mathbf{u}) + \nabla p = -\rho \nabla \phi,$$

$$\frac{\partial E}{\partial t} + \nabla \cdot [\mathbf{u}(E + p)] = -\rho \mathbf{u} \cdot \nabla \phi, \tag{3}$$

$$\frac{\partial (x\rho)}{\partial t} + \nabla \cdot (x\rho \mathbf{u}) = 0,$$

where,

   ρ is the gas mass density $[\mathrm{g\,cm^{-3}}]$,
   $\mathbf{u}$ is the gas velocity $[\mathrm{cm\,s^{-1}}]$,
   p is the pressure $[\mathrm{g\,cm^{-1}\,s^{-2}}]$,
   ϕ is the gravitational potential $[\mathrm{erg\,g^{-1}}]$,
   E is the energy density (including kinetic and internal energy but excluding gravitational potential energy) $[\mathrm{erg\,cm^{-3}}]$,
   x is the ionization fraction [dimensionless].

These equations are modified in the context of an expanding universe. However, a coordinate change described in a later section (Section 7) can be used to return them to the present form.

For simplicity, assume that the gas consists of only hydrogen (helium is neglected). The quantity x is the fraction of the hydrogen gas that is ionized:

$$n_{H^0} = (1 - x)\frac{\rho}{m_H},$$

$$n_{H^+} = x\frac{\rho}{m_H}, \tag{4}$$

where n_{H^0} and n_{H^+} are the number densities of neutral hydrogen atoms and hydrogen ions respectively, and

$$m_H = 1.66 \times 10^{-24}\,\mathrm{g}, \tag{5}$$

is the mass of a hydrogen atom. Due to electrical neutrality, we have

$$n_{e^-} = n_{H^+}. \tag{6}$$

2.3   Thermodynamics

The Euler equations from Eq. 3 need to be closed using the gas equation of state. Since E contains both internal and kinetic energy, we can get the internal energy density e by subtracting the kinetic energy density:

$$e = E - \frac{1}{2}\rho \mathbf{u}^2. \tag{7}$$

The internal energy is related to the pressure by the equation of state:

$$p = (\gamma - 1)e, \tag{8}$$

where we take $\gamma = 5/3$ for a monatomic ideal gas. The temperature is related to the internal energy by

$$e = \frac{3}{2}nk_B T \tag{9}$$

where n is the total number density of all particles contributing to the thermodynamics (H, H^+ and e^-).

$$
\begin{aligned}
n &= n_{H^0} + n_{H^+} + n_{e^-} \\
&= n_{H^0} + 2n_{H^+} \\
&= [(1-x) + 2x]\,\frac{\rho}{m_H} \\
&= (1+x)\frac{\rho}{m_H} \\
&= \frac{\rho}{\mu m_H},
\end{aligned}
\tag{10}
$$

where μm_H is the mean molecular mass. Therefore, the temperature is given by

$$
T = \frac{2}{3}\mu\frac{e}{\rho}\frac{m_H}{k_B}.
\tag{11}
$$

The temperature is modified by various reactions involving the constituent particles of the gas. These include hydrogen atoms, protons, electrons, photons and others. These processes change the internal energy:

$$
\frac{de}{dt} = \Lambda = \mathcal{H} - \mathcal{L},
\tag{12}
$$

where $\mathcal{H}$ and $\mathcal{L}\ [\mathrm{erg\,s^{-1}\,cm^{-3}}]$ are the heating and cooling rates respectively.

The heating and cooling rates contain the details of the various processes. They are computed by the cooling model. We have tested two cooling models in our simulations: RAMSES and ATON. These will be described in a later section.

2.4 Radiative transfer and the M1 approximation

The equation governing radiative transfer is

$$
\frac{1}{c}\frac{\partial I_\nu}{\partial t} + \mathbf{n}\cdot\nabla I_\nu = -\kappa_\nu I_\nu + \eta_\nu,
\tag{13}
$$

where $I_\nu(\mathbf{x}, \mathbf{n}, t)$ is the spectral intensity in $\mathrm{erg\,s^{-1}\,cm^{-2}\,ster^{-1}\,Hz^{-1}}$, $\kappa_\nu(\mathbf{x}, \mathbf{n}, t)$ is the absorption coefficient, and $\eta_\nu(\mathbf{x}, \mathbf{n}, t)$ is the source function.

This equation is complicated because I_ν depends not only on the spacetime coordinates but also on the angle and wavelength. Instead, we will use a simplification described in [1] which depends only on the spacetime coordinates.

To remove the angular dependence, Eq. 13 is first rewritten as an infinite hierarchy of moment equations and the hierarchy is truncated at the third level using the 'M1 approximation'. To remove the frequency dependence, the equations are averaged over the wavelength.

The first and second frequency-averaged moments are defined by

$$
\begin{aligned}
n_\gamma(\mathbf{x}) &= \frac{1}{4\pi}\int_{\nu_0}^\infty d\nu\,\frac{1}{h\nu}\int_{d\Omega} I_\nu(\mathbf{x}, \Omega, t), \\
\mathbf{F}_\gamma(\mathbf{x}) &= \frac{c}{4\pi}\int_{\nu_0}^\infty d\nu\,\frac{1}{h\nu}\int_{d\Omega} \mathbf{n} I_\nu(\mathbf{x}, \Omega, t).
\end{aligned}
\tag{14}
$$

Using Eq. 13, the moments satisfy these equations:

$$
\begin{aligned}
\frac{\partial n_\gamma}{\partial t} + \nabla\cdot\mathbf{F}_\gamma &= -\Gamma n_\gamma + \dot{n}_\gamma, \\
\frac{\partial \mathbf{F}_\gamma}{\partial t} + c^2\partial_i\mathbf{P}^i &= -\Gamma n_\gamma,
\end{aligned}
\tag{15}
$$

Species	Notation
electron	e^-
neutral hydrogen	H, H^0, H I
ionized hydrogen	H^+, H II
neutral helium	He, He I
ionized helium I	He^+, H II
ionized helium II	He^{2+}, H III
photon	γ

Table 1: Notation for the various species in the gas.

where Γ is the absorption rate, $\dot{n}$ is the isotropic source, and $\mathbf{P}^i$ is the third moment, a tensor, which couples the first two moments to the rest of the infinite hierarchy. The M1 approximation truncates this hierarchy by imposing an explicit expression for $\mathbf{P}^i$:

$$\mathbf{P} = \left(\frac{1-\chi}{2}\mathbf{I} + \frac{3\chi - 1}{2}\mathbf{u} \otimes \mathbf{u} \right) n_\gamma, \tag{16}$$

where

$$\chi = \frac{3 + 4|\mathbf{f}|^2}{5 + 2\sqrt{4 - 3|\mathbf{f}|^2}},$$
$$\mathbf{f} = \frac{\mathbf{F}_\gamma}{cn_\gamma} = f\mathbf{u}. \tag{17}$$

An interesting thing about the M1 approximation is that it interpolates between then optically thick, diffusive regime when $\chi = 1/3$ and the optically thin, free-streaming regime when $\chi = 1$.

The quantity J_{21} is defined by

$$J_{21}(\nu) = 10^{21} \frac{I_\nu}{\text{erg s}^{-1}\,\text{cm}^{-2}\,\text{ster}^{-1}\,\text{Hz}^{-1}} \tag{18}$$

This this notation is sometimes used for convenience because I_ν is often smaller than $10^{-21}\,\text{erg s}^{-1}\,\text{cm}^{-2}\,\text{ster}^{-1}\,\text{Hz}^{-1}$ in astrophysical systems.

2.5   Star emission model

The most important sources of radiation for cosmological radiative transfer are the stars. We use the model for stellar photon emission described by [3] and [2]. In this model, stars emit photons at a constant rate over their lifetimes. The rate is proportional to the star mass. We used a rate of 4800 ionizing photons per megayear per baryon in the star.

3   Chemistry and cooling physics

The gas consists of several species of particles, most importantly electrons, hydrogen, helium, and the ionized atomic states. The notation for these species are listed in Table 1. These particles and the ionizing photons react through various processes which change the densities and thermal energy of the gas. The chemistry and cooling model describes the reactions.

This section first discusses the physics of all these processes and the qualitative behaviour. Then the specific models used for ATON and RAMSES are described. Finally, these models are compared in a couple of test cases.

3.1 Boltzmann equation

Let n_i denote the number density of species i (usually in units of cm^{-3}). In general, each species has a complicated distribution in phase space. The phase space evolves according to the Boltzmann equation

$$\frac{dn_i(\mathbf{p})}{dt} = \text{collision terms.} \tag{19}$$

For example, a two-body reaction $1 + 2 \to 3 + 4$ gives a collision term like

$$\begin{aligned}
\frac{dn_3(\mathbf{p_3})}{dt} =& \int \frac{d^3p_1}{(2\pi)^3 2E_1(p)} \int \frac{d^3p_2}{(2\pi)^3 2E_2(p)} \int \frac{d^3p_4}{(2\pi)^3 2E_4(p)} \\
& \times \delta^3(\mathbf{p_1} + \mathbf{p_2} - \mathbf{p_3} - \mathbf{p_4})\delta(E_1(\mathbf{p_1}) + E_2(\mathbf{p_2}) - E_3(\mathbf{p_3}) - E_4(\mathbf{p_4})) \\
& \times |\mathcal{M}|^2 (2\pi)^4 n_1(\mathbf{p_1}) n_2(\mathbf{p_2}),
\end{aligned} \tag{20}$$

where $\mathcal{M}$ is the scattering amplitude.

However, since the gas is highly collisional, the momenta of the gas particles approximately have a Maxwell-Boltzmann distribution with temperature T:

$$n_i(\mathbf{p}; T)d\mathbf{p} = n_i \left(\frac{1}{2\pi mkT} \right)^{3/2} \exp\left(-\frac{\mathbf{p}^2}{2mkT} \right) d\mathbf{p}. \tag{21}$$

All the gas particle species have the same temperature. The ionizing photons have a black body distribution fixed at $T_\gamma = 10^5$ K:

$$n_\gamma(\mathbf{p})d\mathbf{p} = \frac{1}{4\pi^3\hbar^3} \frac{1}{e^{pc/kT_\gamma} - 1} d\mathbf{p}. \tag{22}$$

These distributions allow us to replace $n_i(\mathbf{p})$ with two moments, the total number density and the thermal energy density:

$$\begin{aligned}
n_i &= \int d^3p\, n(\mathbf{p}), \\
e_i &= \begin{cases} \int d^3p\, \frac{p^2}{2m} n(\mathbf{p}) & \text{for gas particles,} \\ \int d^3p\, pc\, n(\mathbf{p}) & \text{for photons.} \end{cases}
\end{aligned} \tag{23}$$

The Boltzmann equation then becomes

$$\begin{aligned}
\frac{dn_3}{dt} &= \langle v_{\text{relative}}\, \sigma \rangle\, n_1 n_2, \\
\frac{de}{dt} &= \langle \Delta E\, v_{\text{relative}}\, \sigma \rangle\, n_1 n_2 = \Lambda.
\end{aligned} \tag{24}$$

The quantities $\langle v_{\text{relative}}\, \sigma \rangle$ and $\langle \Delta E\, v_{\text{relative}}\, \sigma \rangle$ represent the complicated integrals evaluated under the assumed distribution at a particular density and temperature.

The simplified Boltzmann equations of Eq. 24 have an intuitive physical interpretation. Consider a cylinder with base area A containing stationary particles of species 1 as in Fig. 2. Each species 1 particle represents a target of cross-sectional area σ. Suppose a single particle of species 2 moves through the cylinder at speed v_{relative}. After time Δt, it has a chance to hit $N_1 = A v_{\text{relative}} \Delta t\, n_1$ targets. The probability that particle 2 hits one of the targets is equal to the fraction of area covered by the targets, $N_1\sigma/A$. However, since there are $n_2 V$ particles, the total number of events is

$$\Delta N_3 = n_2 V \times v_{\text{relative}} \Delta t\, n_1 \sigma. \tag{25}$$

The rate is therefore

$$\frac{\Delta N_3}{V\Delta t} = v_{\text{relative}}\, \sigma\, n_1 n_2. \tag{26}$$

If each collision transfers ΔE energy into the gas, the cooling rate is

$$\frac{\Delta E_3}{V\Delta t} = \Delta E\, v_{\text{relative}}\, \sigma\, n_1 n_2. \tag{27}$$
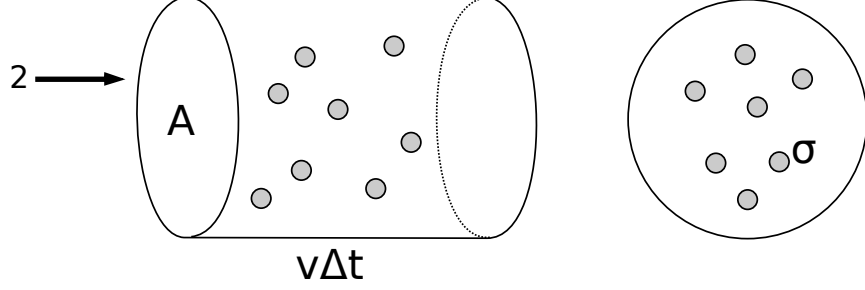
Figure 2: The probability that the single particle 2 collides with one of the species 1 particles is $v_{\text{relative}} \Delta t \, n_1 \sigma$.

3.2 Physical processes

This section describes the particle interaction processes that are included in the ATON model. The model is similar to that used by other cosmological codes like TRAPHIC [18] and TreeSPH [14].

3.2.1 Photoionization: $\gamma + H^0 \to H^+ + e^-$

The main way that which radiation couples to the gas is through photoionization. In a photoionization event, an energetic photon is absorbed by a neutral hydrogen atom causing it to be ionized. The photon must have at least $E_i = 13.6\,\text{eV}$ energy to free the electron.

The cross section for this process depends on the photon energy. It is given by a fit from [21]:

$$\sigma(E) = \sigma_0 \left(\frac{E}{E_0} - 1 \right)^2 \left(\frac{E}{E_0} \right)^{0.5P - 5.5} \left(1 + \sqrt{\frac{E}{E_0 y_a}} \right)^{-P}, \tag{28}$$

where $\sigma_0 = 5.475 \times 10^{-14}\,\text{cm}^2$, $E_0 = 0.4298$, $P = 2.963$, $y_a = 32.88$. This is shown in Fig. 3. We assume the photons have a $10^5\,\text{K}$ blackbody spectrum as shown in Fig. 4. The averaged reaction rate is

$$\frac{dn_{H^+}}{dt} = \int_{E_i}^{\infty} dE \, c \, \sigma(E) \, n_\gamma(E) \, n_{H^0} = c \sigma_\gamma n_\gamma n_{H^0} = \alpha_i n_\gamma n_{H^0}, \tag{29}$$

where $\sigma_\gamma = 1.63 \times 10^{-18}\,\text{cm}^2$ [1].

In a photoionization event, 13.6 eV of the photon energy is used to ionize the atom but any excess energy becomes kinetic energy in the reaction products, heating the gas. The averaged heating rate is given by

$$\frac{de}{dt} = \mathcal{H}_\gamma = n_{H^0} \int_{E_i}^{\infty} dE \, c \, \sigma_\gamma(E) \, n_\gamma(E) \, (E - E_i) \tag{30}$$

$$= n_{H^0} n_\gamma (c \, \sigma_e \, E_e - c \, \sigma_\gamma \, E_i),$$

where $\sigma_e = 1.09691 \times 10^{-18}\,\text{cm}^2$, $E_e = 29.6099\,\text{eV}$ and $E_i = 13.6\,\text{eV}$ [1].

3.2.2 Collisional recombination: $H^+ + e^- \to H^0 + \gamma$

When a proton and electron collide, they can bind together to form a neutral hydrogen atom. The recombined atom can be any of its energy states. It's useful to distinguish two cases for the rates. In Case A recombination, the resulting atom can be in any energy state. In Case B recombination, the atom can be in any state except the ground state. The average rates for the two cases are

$$\alpha_A = 1.27 \times 10^{-13} \, \lambda^{1.503} (1 + (\lambda/0.522)^{0.470})^{-1.923} \ \text{cm}^3\text{s}^{-1},$$
$$\alpha_B = 2.75 \times 10^{-14} \, \lambda^{1.5} (1 + (\lambda/2.740)^{0.407})^{-2.242} \ \text{cm}^3\text{s}^{-1}, \tag{31}$$
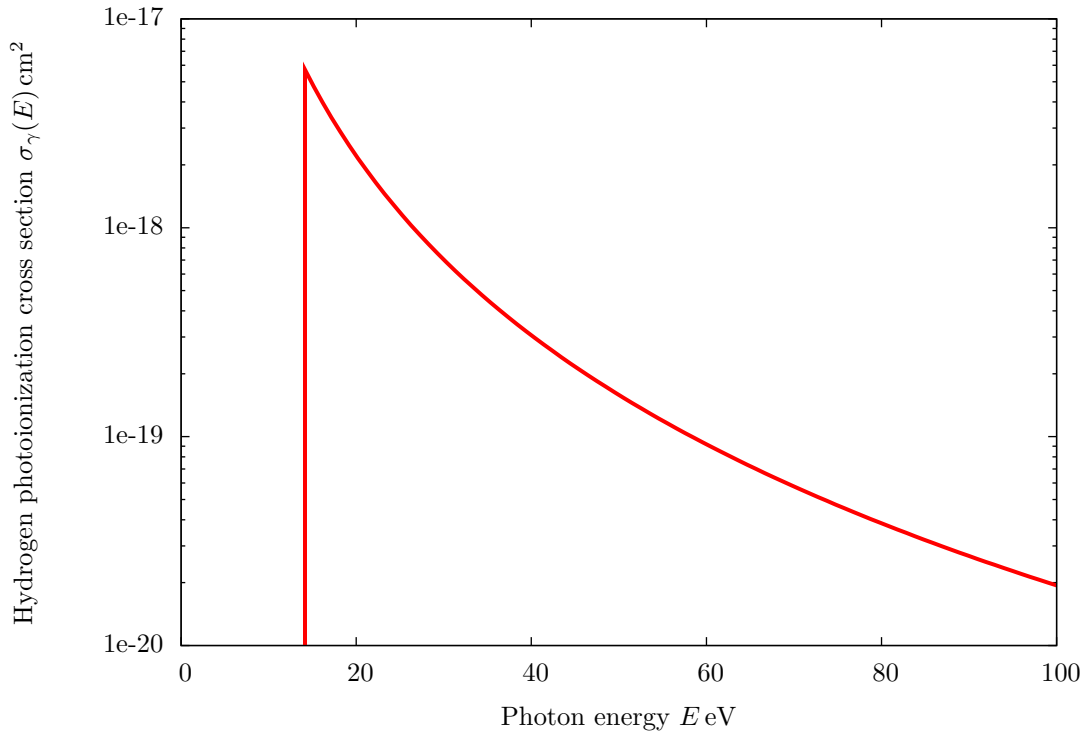
9

Figure 3: The cross section for photoionization of a neutral hydrogen atom by an energetic photon. This is a plot of Eq. 28 as provided by [21].
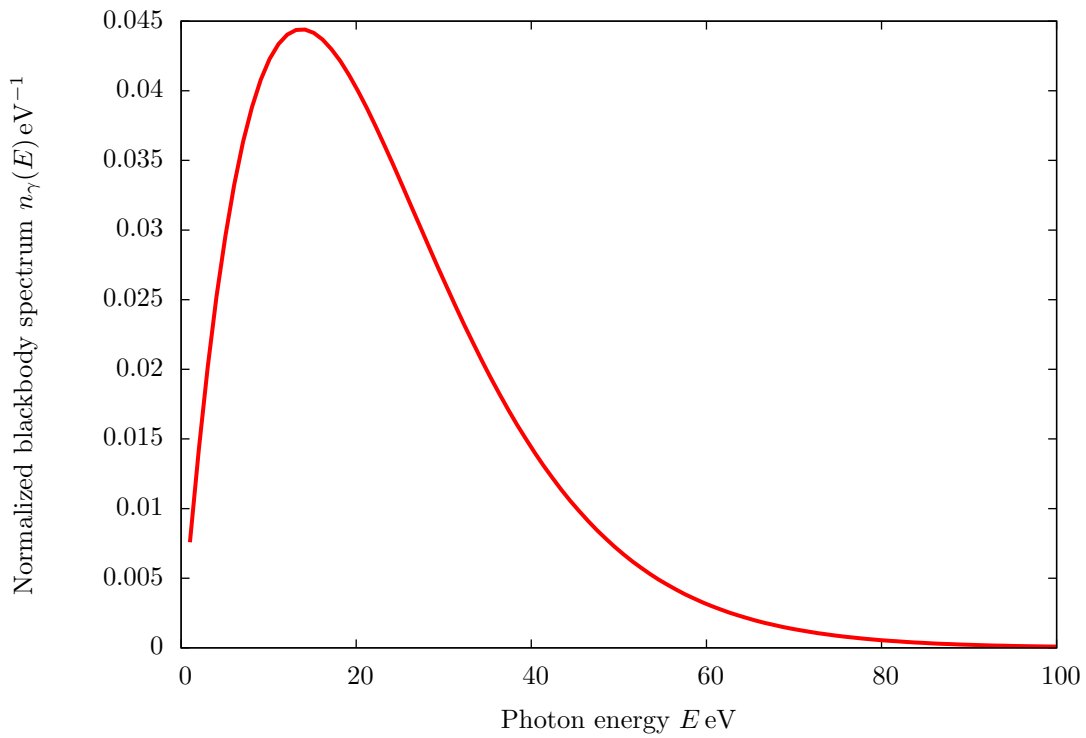

Figure 4: The 10^5 K blackbody spectrum of the photons.

where $\lambda = 2 \times 157807/T$ [12].

If the ions recombine to the ground state then the outgoing photon has enough energy to ionize another neutral atom. This happens very quickly and approximately cancels out the recombination event so that the 'effective' recombination rate is closer to α_B. In the **"On The Spot Approximation"** (OTSA), the recombination rate is directly set to α_B. Our simulations do not use this approximation except in Section 6.2 where it is used for comparison against other codes.

Recombination causes the gas to cool because the number of gas particles decreases and some kinetic energy is transferred to the photon. The cooling rate from [12] is

$$\mathcal{L}_1 = 1.78 \times 10^{-29} \, T \, \lambda^{1.965} (1 + (\lambda/0.541)^{0.502})^{-2.697} n_{e^-} n_{H^+} \; \text{erg cm}^{-3} \text{s}^{-1} \tag{32}$$

3.2.3 Collisional ionization: $e^- + H^0 \to H^+ + e^- + e^-$

The collisional ionization rate from [6] is

$$\beta = 5.85 \times 10^{-11} \, T^{1/2} (1 + T_5^{1/2})^{-1} \exp(-157809/T) \; \text{cm}^3 \text{s}^{-1}, \tag{33}$$

where $T_5 = T/10^5$. The reverse reaction is not significant because it's a three-body process.

For each collisional ionization event, $13.6\,\text{eV}$ is needed to ionize the atom. This energy comes from the kinetic energy of the reactants and therefore reduces the gas temperature.

$$\begin{aligned}
\mathcal{L}_2 &= \beta \times (13.6\,\text{eV}) \\
&= 1.27 \times 10^{-21} \, T^{1/2} (1 + T_5^{1/2})^{-1} \exp(-157809.1/T) n_{e^-} n_{H^0} \; \text{erg cm}^{-3} \text{s}^{-1}
\end{aligned} \tag{34}$$

3.2.4 Collisional excitation cooling

In this process, an electron collides with a neutral atom in the ground state and excites it into a higher state such as $n = 2$. The atom then quickly falls back to the ground state by emitting a photon. For example, it can transition from $n = 2$ to $n = 1$ by emitting a $10.2\,\text{eV}$ Lyman α photon. This doesn't change the densities of the species (since we count only ionizing photons) but the gas is cooled because energy is carried off by the photon. The average cooling rate is given by [6]:

$$\mathcal{L}_3 = 7.5 \times 10^{-19} \exp(-118348/T)(1 + T_5^{1/2})^{-1} n_{e^-} n_{H^0} \; \text{erg cm}^{-3} \text{s}^{-1} \tag{35}$$

3.2.5 Bremsstrahlung cooling

Bremsstrahlung is radiation emitted from electrons when they are decelerated by the hydrogen ions. Since the electrons are slowed, the gas is cooled. The average cooling rate is given by [6]:

$$\mathcal{L}_4 = 1.42 \times 10^{-27} \, (1.5) \, T^{1/2} n_{e^-} n_{H^+} \; \text{erg cm}^{-3} \text{s}^{-1} \tag{36}$$

3.2.6 Compton cooling and heating

The cosmic microwave background (CMB) consists of photons with a blackbody spectrum of temperature $T_{\text{CMB}} = 2.727\,\text{K}/a$. The CMB photons and electrons interact through Compton scattering (where photons have higher energies than the electrons) and inverse Compton scattering (where electrons have higher energies than the photons). This either heats or cools the gas towards the CMB temperature. The average rate given by [17] is:

$$\mathcal{L}_5 = 1.017 \times 10^{-37} \left(\frac{2.727}{a}\right)^4 \left(T - \frac{2.727}{a}\right) n_{e^-} \; \text{erg cm}^{-3} \, \text{s}^{-1}. \tag{37}$$

3.3 Rate equations

The final rate equations for the species densities and gas temperature are found by adding the terms for all these processes. Since we have ignored helium, the only charged species are the electrons and hydrogen ions. By charge conservation, $n_{e^-} = n_{H^+}$. Also, the number of protons is conserved so $n_H = n_{H^0} + n_{H^+}$ is constant. Therefore, we only need to track n_γ and the ionized fraction x.

The rate equation for the ionizing photon density includes photoionization and recombination:

$$\frac{dn_\gamma}{dt} = -n_{H^0} n_\gamma \alpha_i + n_{e^-} n_{H^+} (\alpha_A - \alpha_B). \tag{38}$$

The factor $(\alpha_A - \alpha_B)$ is used instead of just α_A for recombination because n_γ counts only ionizing photons.

According to Eq. 15, the photon flux is also decreased by photoionization absorption:

$$\frac{d\vec{F}_\gamma}{dt} = -n_{H^0} \alpha_i \vec{F}_\gamma. \tag{39}$$

It is not affected by recombination because the photons are emitted isotropically.

The rate equation for the neutral hydrogen density includes photoionization, recombination and collisional ionization:

$$\frac{dn_{H^0}}{dt} = n_{e^-} n_{H^+} \alpha_A - n_{e^-} n_{H^0} \beta - n_\gamma n_{H^0} \alpha_i. \tag{40}$$

This can be written in terms of the ionized fraction:

$$\frac{dx}{dt} = -x^2 n_H \alpha_A + x(1-x) n_H \beta + n_\gamma (1-x) n_H \alpha_i. \tag{41}$$

The thermal gas energy evolves according to

$$\frac{de}{dt} = \Lambda = \mathcal{H} - \sum_{i=1}^{5} \mathcal{L}_i, \tag{42}$$

where $\mathcal{H}$ is the photoionization heating rate and and $\mathcal{L}_i$ are all the cooling rates.

3.4 Qualitative behaviour

Often the universe is close to the photoionization equilibrium regime where x is almost constant. The equilibrium ionized fraction can be found be setting $dx/dt = 0$ in Eq. 41:

$$0 = x_{\text{eq}}^2 (\alpha_A + \beta) + x_{\text{eq}} \left(\frac{n_\gamma}{n_H} \alpha_i - \beta \right) - \frac{n_\gamma}{n_H} \alpha_i. \tag{43}$$

Notice that the equilibrium ionized fraction depends on the photon density only through the factor n_γ/n_H. Fig. 5 and Fig. 6 show the equilibrium ionized fraction as a function of T and n_γ/n_H. Qualitatively, we see that the gas becomes strongly ionized when $T > 10^4$ K or when n_γ/n_H is large (depending on the temperature).

In the limit where n_γ/n_H is small, the equilibrium ionized fraction from Eq. 43 simplifies to

$$x_{\text{eq}} = \frac{\beta}{\alpha_A + \beta}. \tag{44}$$

So x_{eq} depends only on the temperature, not on n_γ/n_H, in this limit. Since only collision ionization processes contribute, this limit is called **collisional ionization equilibrium** (CIE). Fig. 5 shows the CIE ionized fraction as a function of T.
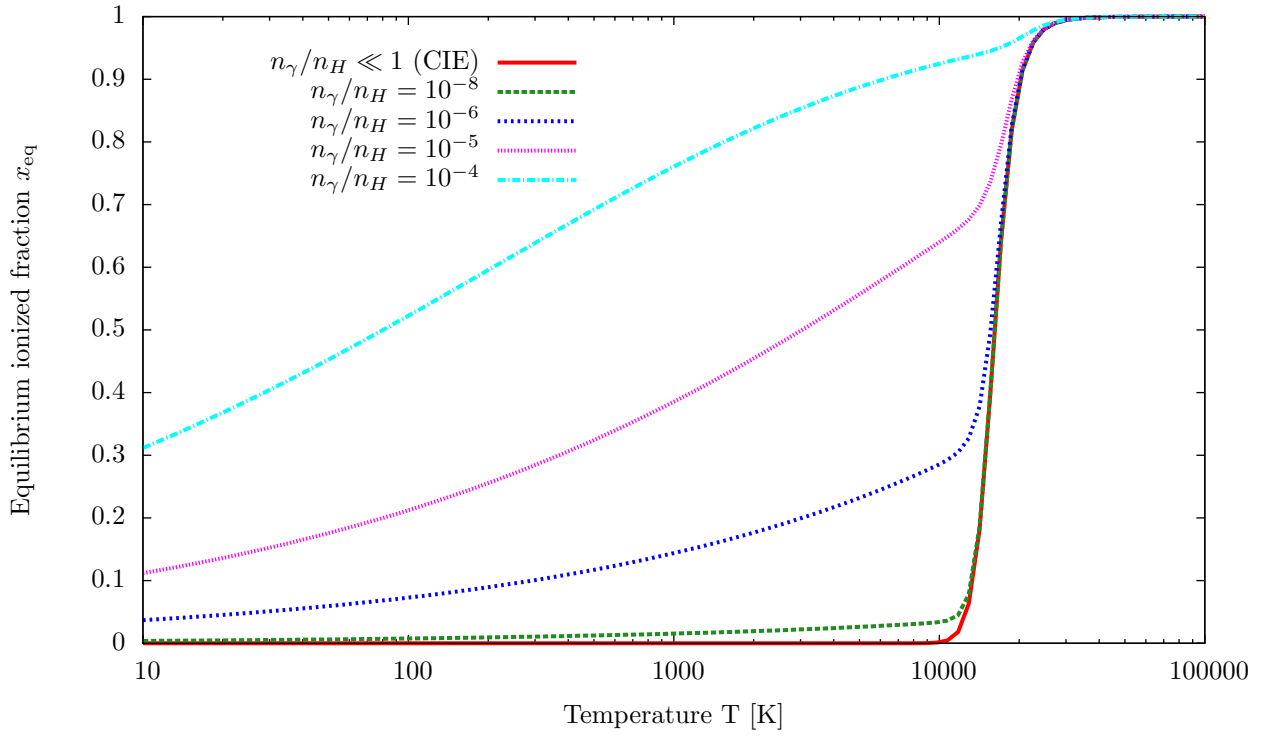
Figure 5: The equilibrium ionized fraction from Eq. 43 as a function of temperature.
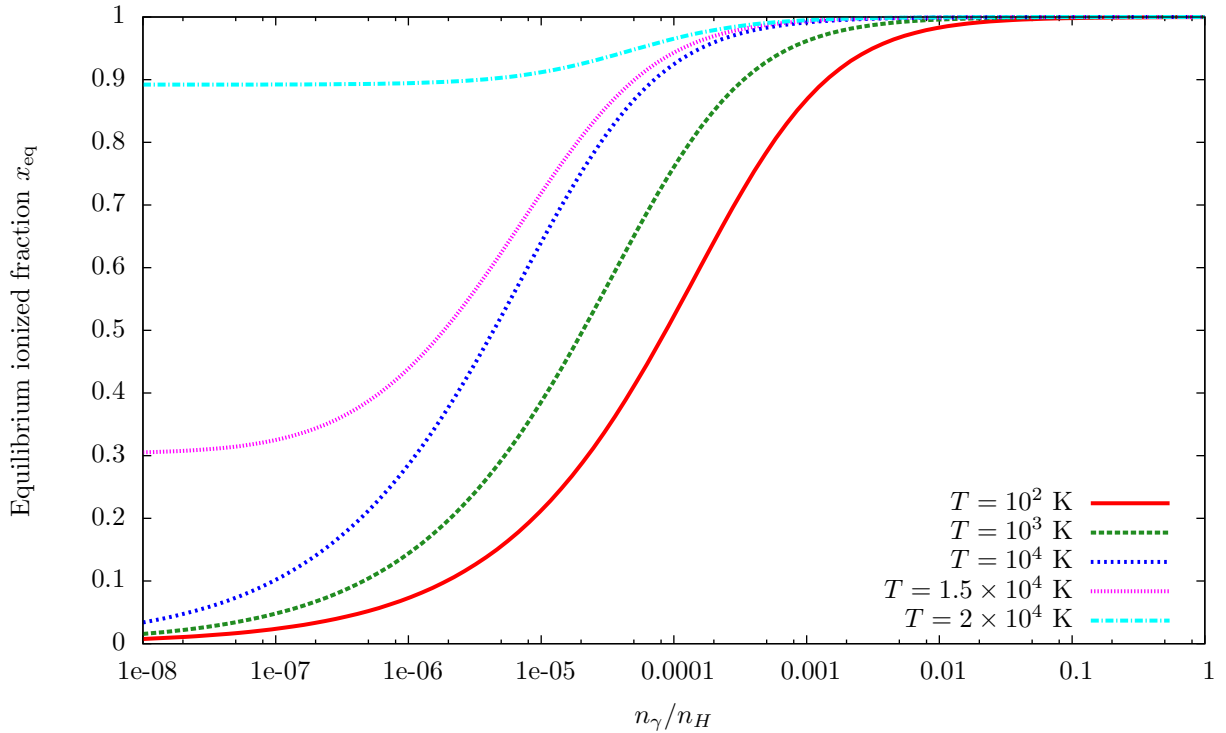
Figure 6: The equilibrium ionized fraction from Eq. 43 as a function of n_γ/n_H.
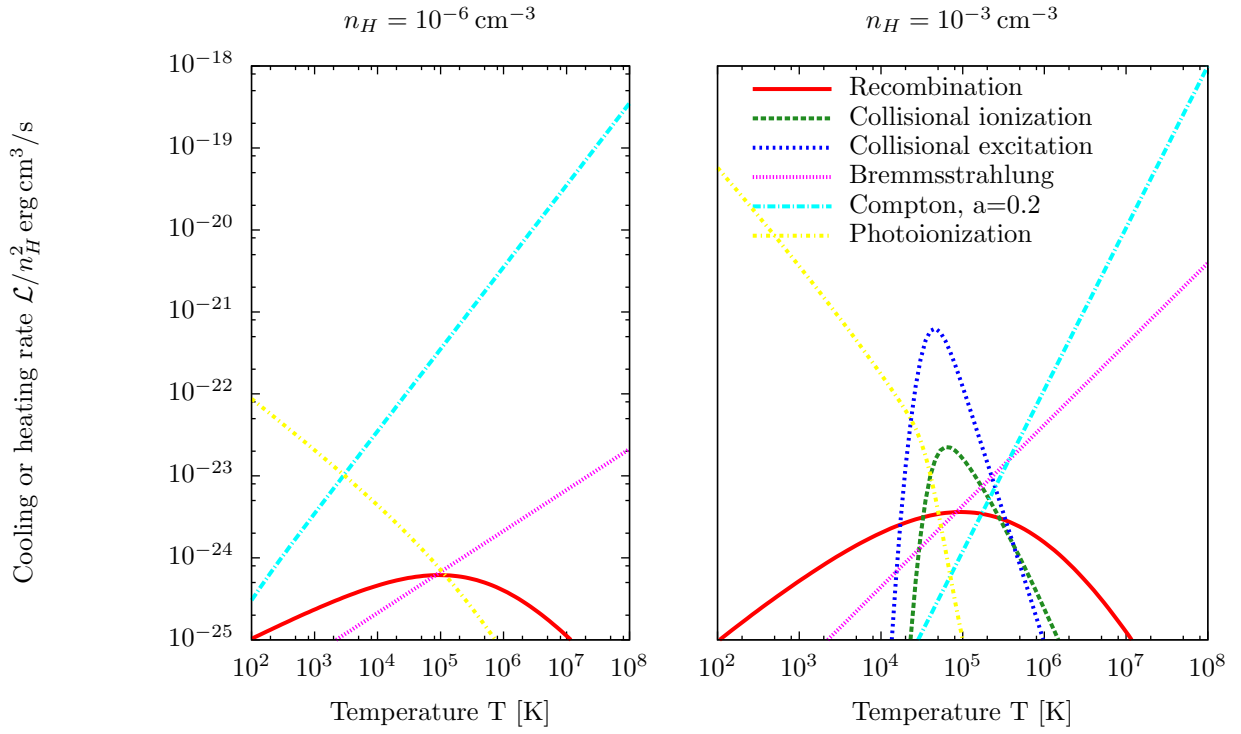
Figure 7: Cooling and heating rates when $n_\gamma = 6.3 \times 10^{-6}$ and $a = 0.2$. This photon density is the typical cosmological background value after reionization. The rates are all calculated using the equilibrium ionization fraction. These plots are comparable to those in [14].
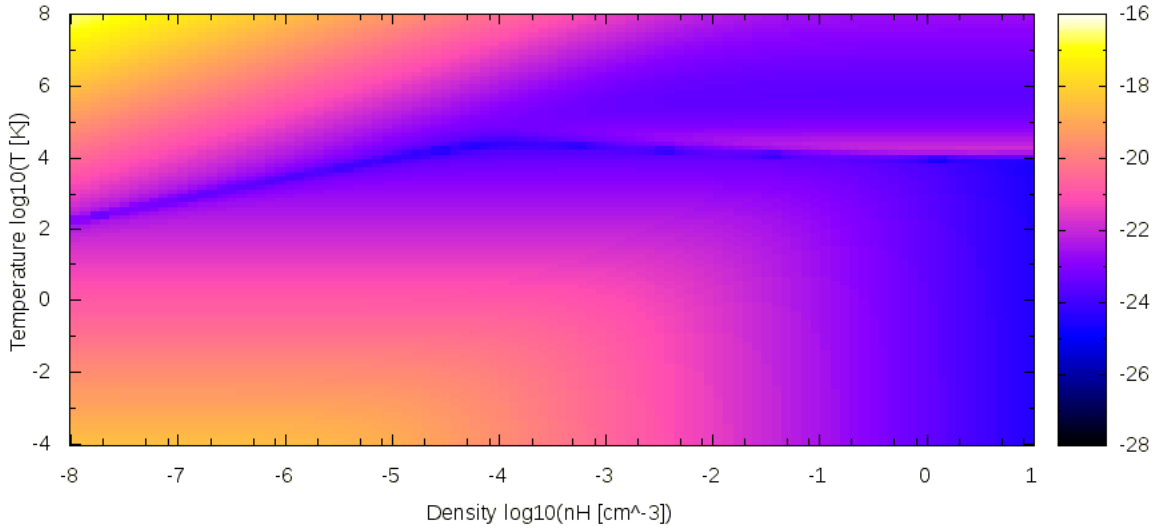
Figure 8: Net heating and cooling rate $|\mathcal{H} - \mathcal{L}|$ as a function of both T and n_H using $n_\gamma = 6.3 \times 10^{-6}$, $a = 0.2$ and the equilibrium ionization fraction.

14
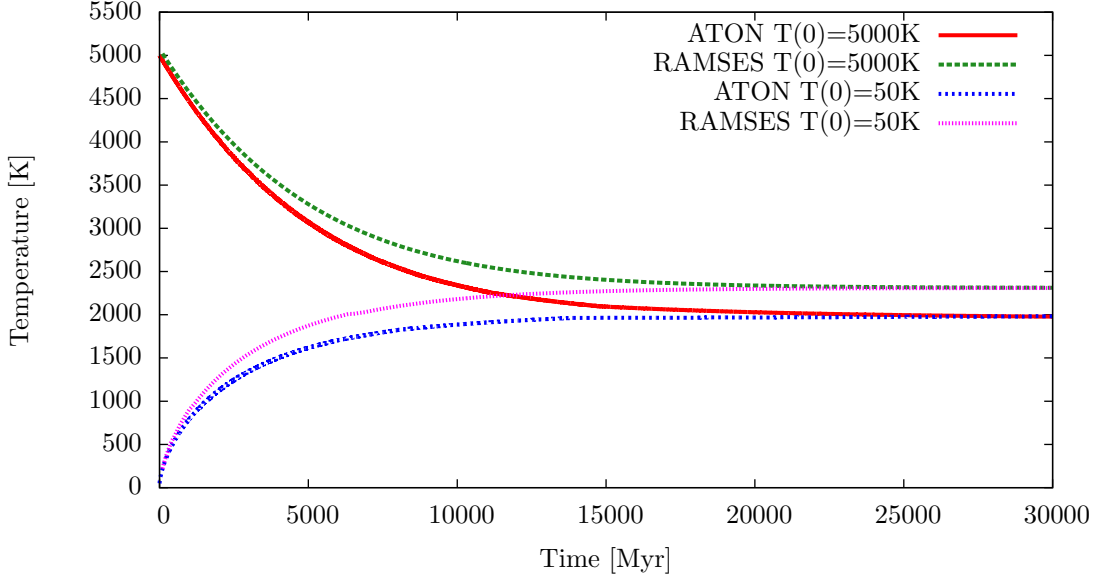
Figure 9: The temperature evolution computed by the RAMSES and ATON cooling models. Initial conditions: $n_H = 3 \times 10^{-7}\,\text{cm}^{-3}$, $1 - x = 10^{-6}$, $J_{21} = 0.1$, redshift $z = 11.5$, with $T_2 = 10^4\,\text{K}$ and $T_2 = 10^2\,\text{K}$.

Fig. 7 shows the various cooling rates as a function of temperature for a particular photon density. Collisional excitation cooling dominates near $T = 10^4\,\text{K}$ when $n_H = 10^{-3}\,\text{cm}^{-3}$ but is completely absent when $n_H = 10^{-6}\,\text{cm}^{-3}$. Compton cooling dominates at low densities.

Fig. 8 shows the net heating and cooling rate as a function of both T and n_H. The equilibrium temperature contour can be seen where the net rate tends to zero. At high densities, there is a valley near $10^6\,\text{K}$ where cooling is quite inefficient. When $n_H > 0.1\,\text{cm}^{-3}$, heating also becomes inefficient.

All the cooling rates (except Compton cooling) are proportional to n_H^2. The thermal energy density is proportional to n_H. Therefore, the cooling time scale is proportional to

$$t_{\text{cool}} \sim \frac{e}{\Lambda} \sim \frac{1}{n_H}. \tag{45}$$

Cooling is faster at high densities.

3.5   Chemical equilibrium cooling

RAMSES uses a cooling model which differs from the one described so far in two important respects. Firstly, it includes cooling processes involving helium. Secondly, instead of evolving the ionization fractions, it assumes that the gas is always in chemical equilibrium. For a given temperature and density, it firsts calculates the ionization fractions and computes the rates according to these. The procedure is described in [14]. Chemical equilibrium is usually a good approximation but it can give quite different results in some situations. To illustrate this, we compare the temperature computed by the two models in two tests.

The first test uses a low density ($n_H \approx 10^{-7}\,\text{cm}^{-3}$) and moderate initial photon flux ($n_\gamma = 6.3 \times 10^{-6}\,\text{cm}^{-3}$). The results are shown in Fig. 9. Both models give similar results in this case.

The second test uses a higher density $n_H \approx 10^{-4}\,\text{cm}^{-3}$ and higher photon flux ($n_\gamma = 6.3 \times 10^{-4}\,\text{cm}^{-3}$). The gas is initially neutral. The results are shown in Fig. 10. The temperature jumps instantaneously to its final value for the non-equilibrium (ATON) model. The temperature increases very slowly in the RAMSES model. Since $n_\gamma/n_H \approx 1$, RAMSES thinks that the gas is already fully ionized at the start of the test. Therefore the photoionization heating rate is low. On the other hand, the non-equilibrium model sees the gas as initially neutral so the heating rate is very high.
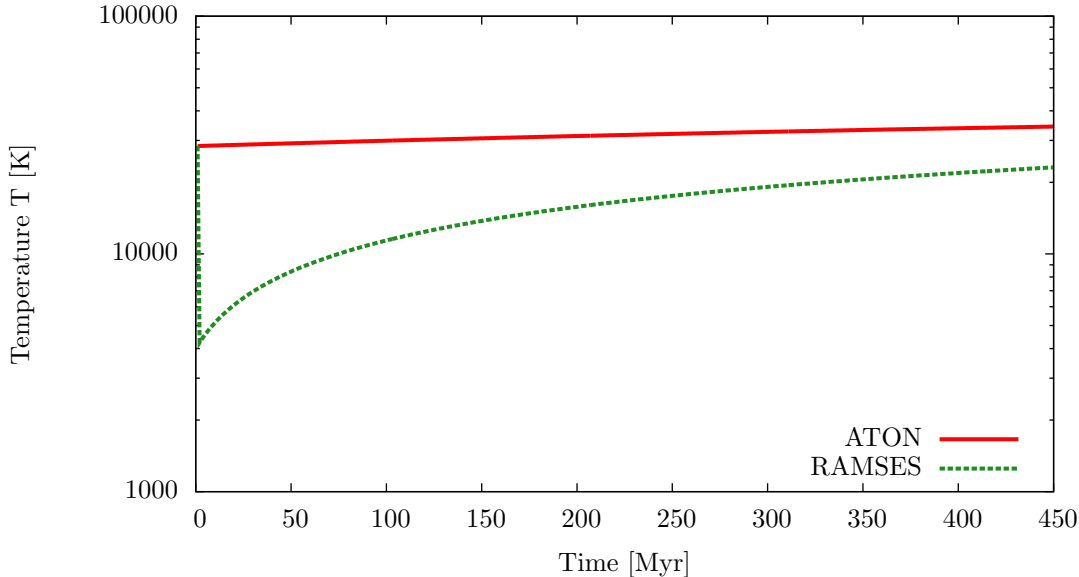
Figure 10: The temperature evolution computed by the ATON and RAMSES cooling models for the initial conditions: $n_H = 2 \times 10^{-4}\,\mathrm{cm}^{-3}$, $x = 0$, $J_{21} = 10$, redshift $z = 0$, and $T_2 = 8000\,\mathrm{K}$.

4   Numerical methods

4.1   Godunov scheme for hyperbolic systems of conservation laws

Both the Euler equations (Eq. 3) and the radiative transfer moment equations in the M1 approximation (Eq. 15) are hyperbolic systems of conservation laws (if the source terms are neglected). Such equations can be solved effectively using Godunov methods. In this section, we will briefly describe the Godunov method and its implementation in ATON.

To simplify the discussion, first consider the equations in one dimension. Both the Euler equations and the M1 moment equations can be written in the form

$$\partial_t \mathbf{u} + \partial_x \mathbf{f}(\mathbf{u}) = 0, \tag{46}$$

where $\mathrm{u}(x,t)$ is the vector of conserved quantities and $\mathbf{f}(\mathbf{u})$ is the flux function. The conservation laws can be found by integration:

$$\begin{aligned}
0 &= \partial_t \mathbf{u} + \partial_x \mathbf{f}(\mathbf{u}) \\
&= \int_a^b dx \int_0^\tau dt\, [\partial_t \mathbf{u} + \partial_x \mathbf{f}(\mathbf{u})] \\
&= \int_a^b dx\, [\mathbf{u}(x,\tau) - \mathbf{u}(x,0)] + \int_0^\tau dt\, [\mathbf{f}(\mathbf{u}(b,t)) - \mathbf{f}(\mathbf{u}(a,t))].
\end{aligned} \tag{47}$$

The interpretation is that the total quantity within the interval $[a, b]$ changes only by transportation through the boundary.

In order to solve this equation numerically, space is discretized into cells of size Δx. The cell-averaged quantities $\mathbf{u}_i^n$ are defined by

$$\mathbf{u}_i^n = \int_{(i-\frac{1}{2})\Delta x}^{(i+\frac{1}{2})\Delta x} dx\, \mathbf{u}(x). \tag{48}$$
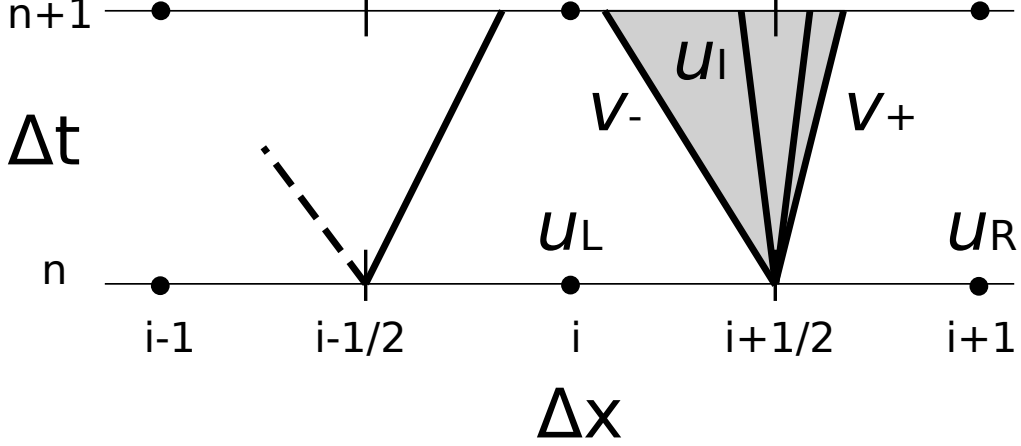
16

Figure 11: Several waves are emitted from the step discontinuity at an averaged cell interface in the solution to the Riemann problem.

The projected solution $\mathbf{v}_n(x,0)$ is defined by

$$\mathbf{v}_n(x,0) = \mathbf{u}_i^n, \quad \text{if} \ \left(i - \frac{1}{2}\right)\Delta x < x < \left(i + \frac{1}{2}\right)\Delta x. \tag{49}$$

If we zoom into a cell boundary, $\mathbf{v}(x,0)$ looks like a step function. Eq. 46 with a step discontinuity initial condition is called the Riemann problem. The Riemann problem can actually be solved exactly. By patching together the solutions at each cell boundary, the evolution of the projected solution $\mathbf{v}_n(x,t)$ can be obtained. Of course, this only works if t is small enough that the adjacent Riemann solutions don't overlap. The projected solution $\mathbf{v}_n(x,\Delta t)$ can then be averaged to find an approximation of $\mathbf{u}_i^{n+1}$. This is Godnuov's method.

It is simpler and sometimes sufficient to use an approximate solution of the Riemann problem instead of the exact solution. One such approximate scheme is the Harten, Lax and van Leer (HLL) method [11]: Consider the Riemann problem at the $i + 1/2$ cell interface in Fig. 11. The discontinuity will produce several waves and shocks which each move away from the interface at different velocities. Let v_- and v_+ be the minimum and maximum velocities. This divides the solution into three regions: left, right and the interior. The left and right regions are not affected by the waves so the solution is constant and equal to the original cell value. The interior solution is complicated in general. The HLL method approximates the interior solution by a constant value. The approximate projected solution is

$$\mathbf{v}_n(x,t) = \begin{cases} \mathbf{u}_L & \text{if } x < (1+1/2)\Delta x + v_- t, \\ \mathbf{u}_I & \text{if } (i+1/2)\Delta x + v_+ t < x < (1+1/2)\Delta x + v_- t, \\ \mathbf{u}_R & \text{if } x > (i+1/2)\Delta x + v_+ t. \end{cases} \tag{50}$$

The value $\mathbf{u}_I$ can be calculated by applying the conservation law around the cell rectangle $[i, i+1] \times [n, n+1]$:

$$0 = \int_{i\Delta x}^{(i+1)\Delta x} dx \left[\mathbf{v}(x, (n+1)\Delta t) - \mathbf{v}(x, n\Delta t)\right] + \int_{n\Delta t}^{(n+1)\Delta t} dt \left[\mathbf{f}(\mathbf{u}((i+1)\Delta x, t)) - \mathbf{f}(\mathbf{u}(i\Delta x, t))\right]$$

$$= \mathbf{u}_L(\Delta x/2 + v_-\Delta t) + \mathbf{u}_I(v_+\Delta t - v_-\Delta t) + \mathbf{u}_R(\Delta x/2 - v_+\Delta t) - (\mathbf{u}_L + \mathbf{u}_R)\Delta x/2 + \Delta t\,\mathbf{f}(\mathbf{u}_R) - \Delta t\,f(\mathbf{u}_L)$$

$$\mathbf{u}_I = \frac{\mathbf{u}_R v_+ - \mathbf{u}_L v_-}{v_+ - v_-} + \frac{\mathbf{f}(\mathbf{u}_L) - \mathbf{f}(\mathbf{u}_R)}{v_+ - v_-}. \tag{51}$$

The Godunov scheme written in its conservative form is

$$\mathbf{u}_i^{n+1} = \mathbf{u}_i^n - \frac{\Delta t}{\Delta x}(\mathbf{f}_{i+1/2} - \mathbf{f}_{i-1/2}). \tag{52}$$

The interface fluxes can be calculated by applying the conservation law using the approximate solution around the half-cell rectangle $[i, i + 1/2] \times [n, n + 1]$:

$$\int_{i\Delta x}^{(i+1/2)\Delta x} dx\, \mathbf{v}(x, (n + 1)\Delta t) - \frac{\Delta x}{2}\mathbf{u}_L + \int_{n\Delta t}^{(n+1)\Delta t} dt\, \mathbf{f}(\mathbf{v}((i + 1/2)\Delta x, t)) - \Delta t\, \mathbf{f}(\mathbf{u}_L) = 0. \quad (53)$$

Note that $\mathbf{f}(\mathbf{v}((i + 1/2)\Delta x, t))$ is constant, independent of t. It can be identified as $\mathbf{f}_{i+1/2}$ from Eq. 52. Solving for $\mathbf{f}_{i+1/2}$, we find:

$$\mathbf{f}_{i+1/2} = \frac{-v_-\mathbf{f}(\mathbf{u}_R) + v_+\mathbf{f}(\mathbf{u}_L) + v_+v_-(\mathbf{u}_R - \mathbf{u}_L)}{v_+ - v_-}. \quad (54)$$

We still need to calculate v_- and v_+. The HLL method in its original form [11] doesn't specify a particular way to do this. One way is to linearize Eq. 46:

$$\partial_t\mathbf{u} + \left(\frac{\partial\mathbf{f}}{\partial\mathbf{u}}\right)_{\mathbf{u}_0}\cdot\partial_x\mathbf{u} = 0. \quad (55)$$

The eigenvalues of the Jacobian correspond to the initial wave speeds. Another option is to simply use the maximum possible speed, c, everywhere:

$$\begin{aligned} v_- &= -c \\ v_+ &= c. \end{aligned} \quad (56)$$

This is called the global Lax Friedrich (GLF) scheme. It's much simpler because we don't need to compute the eigenvalues but it's also less accurate due to numerical dispersion.

All our simulations use the GLF scheme for the M1 radiative transfer solver in ATON. For the Euler equations, RAMSES also uses a Godunov-type method, but not HLL. It uses an almost exact solution to the Riemann problem and a second-order scheme. It also has modifications to account for the gravity source terms.

4.2 Stability of the GLF scheme

In two dimensions, the conservation equations from Eq. 46 for a scalar quantity $u(x, y, t)$ become

$$\begin{aligned} 0 &= \partial_t u + \partial_x f(u) + \partial_y g(u) \\ &= \partial_t u + \frac{df}{du}\partial_x u + \frac{dg}{du}\partial_y u. \end{aligned} \quad (57)$$

Assume that $df/du = c_x$ and $dg/du = c_y$ are constant. Define C_x and C_y by

$$\begin{aligned} C_x &= \frac{c_x\Delta t}{\Delta x}, \\ C_y &= \frac{c_y\Delta t}{\Delta y}. \end{aligned} \quad (58)$$

The GLF scheme is then

$$u_{ij}^{n+1} = (1 - C_x - C_y)u_{ij}^n + C_x u_{i-1,j}^n + C_y u_{i,j-1}^n. \quad (59)$$

To check the stability of the scheme, we use a von Neumann stability analysis. Consider a single Fourier mode $u_i^n = A^n e^{-ik_1 i \Delta x - ik_2 j \Delta y}$:

$$
\begin{aligned}
A^{n+1} &= A^n(1 - C_x - C_y) + A^n C_x e^{ik_1 \Delta x} + A^n C_y e^{ik_2 \Delta y} \\
\frac{A^{n+1}}{A^n} &= [(1 - C_x - C_y) + C_x \cos k_1 \Delta x + C_y \cos k_2 \Delta y] + i [C_x \sin k_1 \Delta x + C_y \sin k_2 \Delta y] \\
\left| \frac{A^{n+1}}{A^n} \right| &= C_x^2 + C_y^2 + (1 - C_x - C_y)^2 + 2(1 - C_x - C_y)(C_x \cos k_1 \Delta x + C_y \cos k_2 \Delta y) \\
&\quad + 2 C_x C_y [\cos k_1 \Delta x \cos k_2 \Delta y + \sin k_1 \Delta x \sin k_2 \Delta y] \\
&= C_x^2 + C_y^2 + (1 - C_x - C_y)^2 + 2(1 - C_x - C_y)(C_x \cos k_1 \Delta x + C_y \cos k_2 \Delta y) \\
&\quad + 2 C_x C_y \cos(k_1 \Delta x - k_2 \Delta y).
\end{aligned}
\tag{60}
$$

If $C_x + C_y < 1$ then the factor is maximised when $k_1 \Delta x = k_2 \Delta y = 0$:

$$
\left| \frac{A^{n+1}}{A^n} \right| \leq C_x^2 + C_y^2 + (1 - C_x - C_y)^2 + 2(1 - C_x - C_y)(C_x + C_y) + 2 C_x C_y = 1.
\tag{61}
$$

Therefore, the scheme is stable if $C_x + C_y < 1$.

In three dimensions with cubic cells, the stability condition becomes

$$
\Delta t < \frac{\Delta x}{3c}.
\tag{62}
$$

5 Implementation

This section describes the details about how the RAMSES and ATON codes were coupled together.

RAMSES handles hydrodynamics, n-body dark matter and star formation. It uses adaptive mesh refinement to improve resolution in critical areas of simulation domain. It is written in Fortran and uses MPI for communication.

ATON consists of two parts: a GLF solver for the radiative transfer moment equations and a cooling and chemistry solver. Unlike RAMSES, it requires a fixed grid. It is written in NVIDIA CUDA (which is based on C++). Most of the new code was written in Fortran because it needs to access the internals of RAMSES. However, it was also necessary to make some changes to the CUDA GPU code.

The essential idea is to split every coarse time step into two parts. The first part is the usual RAMSES coarse time step. The new hydrodynamic quantities are then copied to ATON. ATON then advances many small radiation time steps (since the radiation time step is much smaller than the hydrodynamic time step). The updated quantities are then copied back to RAMSES.

5.1 ATON on the GPU

Running ATON on a GPU instead of a CPU gives a significant $100\times$ speedup [2] which makes the radiative transfer simulations feasible. The variant of ATON written in CUDA is called CUDATON.

Most of our simulations used machines with NVIDIA Tesla S1070 GPUs. Each of these GPUs has 240 lightweight cores which make homogeneous parallel calculations (like advancing a GLF time step) really fast. The major bottleneck is memory bandwidth between the host machine and the GPU. The GPU has its own RAM and any data has to be transferred over a PCIe bus. Therefore, we have to be careful to minimize the transfers.

Double precision floating point numbers are not supported or are slow except on recent NVIDIA GPU models. Therefore, we use single precision for ATON.

Typically a single machine will have several GPUs and the program must explicitly choose which GPU to use by its id. Unfortunately, this means that if multiple programs are to run on the same machine, they must coordinate so that they choose different GPUs. We implemented this using MPI by gathering all the machine hostnames used in the simulation and counting duplicates.

5.2 AMR and fixed grids

RAMSES uses an AMR grid which is in general distributed among the MPI processes in a complicated way. CUDATON requires regular grid and doesn't support networking. To resolve the AMR vs regular grid problem, we choose to only simulate radiation at the coarest AMR level (which is a regular grid). The coarse grid is decomposed into blocks and each block is assigned to one MPI process.

At the start of the ATON time step, we first need to fill the local block using updated quantities from the distributed AMR grid. For each cell in the local grid, we find which CPU holds the AMR values for that position and add it to a request buffer. All the nodes then transfer the requested cells among themselves. The same thing is done in reverse at the end of the time step. Finding the value of a quantity in the AMR grid is a matter of walking down the AMR octree structure until a leaf cell is reached.

One optimization is that the photon flux is only used internally by ATON. Therefore, there is no need to store it in the AMR grid. This saves some RAM and network usage.

5.3 Substepping and boundary memory transfers

The ATON time step (given by the Courant condition of Eq. 62) is typically 100 to 1000 times smaller than the RAMSES time step so we need to run many radiation substeps for each coarse time step.

At each substep, we need to communicate the grid boundary cells between adjacent blocks. Unfortunately, this has to be done via the host and involve GPU memory transfers. It is too slow to transfer each boundary cell separately. Instead, we wrote GPU functions to pack or unpack the boundary cells of a face into a flat buffer which can be transferred as a single unit. Since the moment scheme only depends on n_γ and $\mathbf{F}_\gamma$, only these quantities need to be transferred.

Boundary conditions on the simulation domain are easily implemented by manipulating these buffers as a whole. To set zero-gradient (transmissive) boundary condition on a face, the buffer for that face is simply returned to the GPU without modification. For periodic boundary conditions, the buffers are transferred between opposite faces of the grid.

5.4 Incorporating radiation into the RAMSES cooling module

ATON provides a non-equilibrium hydrogen-only cooling model as described in Section 3. However, it may not be easy to adapt it for use with AMR. RAMSES provides a chemical equilibrium cooling model using both hydrogen and helium which already works with AMR. Therefore, we wanted the option of using either model in our simulations.

The RAMSES cooling model assumes a uniform background photon flux with a power law spectrum and intensity I_0. This spectrum is used to calculate the chemical equilibrium concentrations of the various ions and calculate the heating and cooling rates. The rates are stored in a lookup table for speed. We needed to adapt this model to make use the non-uniform radiation spectrum computed by ATON.

At first glance, it seems like extensive changes will be needed because of the lookup table. In fact, it can be done using an easy trick: The photoionization heating rate $\mathcal{H}/n_H^2$ depends on the radiation intensity only through the factor n_γ/n_H. The ionized fraction also depends on this factor and therefore so do all the cooling rates. The trick is to lookup the heating and cooling rates from the table using an 'effective' density $n'_H = n_H I_0/I_{\mathrm{ATON}}$. This will return the correct rates for the new flux.

We need to convert between the photon density n_γ in units of m^{-3} and I_0 in cgs units $\mathrm{erg\,s}^{-1}\,\mathrm{cm}^{-2}\,\mathrm{ster}^{-1}\,\mathrm{Hz}^{-1}$. RAMSES assumes that the spectrum follows a power spectrum law

$$I_\nu = I_0 \frac{e_L}{e},\tag{63}$$

where

$$I_0 = J_{21} \cdot 10^{-21},\tag{64}$$

$e = h\nu$ and $e_L = 13.598\,\mathrm{eV}$. The ionizing photon number density n_γ can be calculated by integrating the spectrum I_ν:

$$
\begin{aligned}
n_\gamma &= \int_{\nu_L}^{\infty} \mathrm{d}\nu \frac{4\pi I_\nu}{ch\nu}\\
&= \int_{e_L}^{\infty} \frac{\mathrm{d}e}{h} \frac{4\pi I_\nu}{ce}\\
&= \frac{4\pi}{hc} \int_{e_L}^{\infty} \mathrm{d}e \frac{I_0 e_L}{e^2}\\
&= \frac{4\pi}{hc} I_0 e_L \left[-\frac{1}{e} \right]_{e_L}^{\infty}\\
&= \frac{4\pi I_0}{hc}.
\end{aligned}
\tag{65}
$$

The lower limit of integration is e_L because we only want to count ionizing photons. ATON uses SI units where

$$[n_\gamma] = \mathrm{m}^{-3}.\tag{66}$$

In these units:

$$
\begin{aligned}
\left(\frac{n_\gamma}{\mathrm{m}^{-3}}\right)\mathrm{m}^{-3} &= \frac{4\pi\,\mathrm{ster}}{hc}\left(\frac{I_0}{\mathrm{erg\,s}^{-1}\,\mathrm{cm}^{-2}\,\mathrm{ster}^{-1}\,\mathrm{Hz}^{-1}}\right)\mathrm{erg\,s}^{-1}\,\mathrm{cm}^{-2}\,\mathrm{ster}^{-1}\,\mathrm{Hz}^{-1}\\
\left(\frac{n_\gamma}{\mathrm{m}^{-3}}\right) &= \frac{4\pi}{hc}\left(\frac{I_0}{\mathrm{erg\,s}^{-1}\,\mathrm{cm}^{-2}\,\mathrm{ster}^{-1}\,\mathrm{Hz}^{-1}}\right)\mathrm{erg\,s}^{-1}\,\mathrm{cm}^{-2}\,\mathrm{m}^{3}\,\mathrm{Hz}^{-1}\\
&= 4\pi 10^4 \left(\frac{\mathrm{erg\,s}}{h}\right)\left(\frac{\mathrm{m/s}}{c}\right)\left(\frac{I_0}{\mathrm{erg\,s}^{-1}\,\mathrm{cm}^{-2}\,\mathrm{ster}^{-1}\,\mathrm{Hz}^{-1}}\right)\mathrm{s}^{-1}\,\mathrm{Hz}^{-1}\\
&= 4\pi 10^4 \frac{1}{6.626\times10^{-27}}\frac{1}{2.998\times10^{8}}\left(\frac{I_0}{\mathrm{erg\,s}^{-1}\,\mathrm{cm}^{-2}\,\mathrm{ster}^{-1}\,\mathrm{Hz}^{-1}}\right)\\
\left(\frac{n_\gamma}{\mathrm{m}^{-3}}\right) &= 6.326\times10^{22}\left(\frac{I_0}{\mathrm{erg\,s}^{-1}\,\mathrm{cm}^{-2}\,\mathrm{ster}^{-1}\,\mathrm{Hz}^{-1}}\right).
\end{aligned}
\tag{67}
$$

5.5 Modes of operation

There are several modes of operation of the new code. The ATON chemistry and cooling model is always used to evolve the photon density and ionized fraction. However, the temperature can be controlled either by the ATON model or by the RAMSES model.

1. ATON cooling model mode: The temperature is controlled by the ATON cooling model.

2. RAMSES cooling model mode: The temperature is controlled by the RAMSES cooling model. The ATON model is still used to evolve the photon density and ionized fraction.

3. No radiation feedback mode: The temperature is controlled by the RAMSES model but it uses a constant background photon density instead of the value computed by ATON. Therefore, radiation doesn't affect the hydro simulation at all. The radiation is still simulated within ATON but with the temperature fixed at $10^4\,\mathrm{K}$.

4. Radiation disabled mode: In this mode, the radiation code is completely disabled and the simulations is identical to unmodified RAMSES.
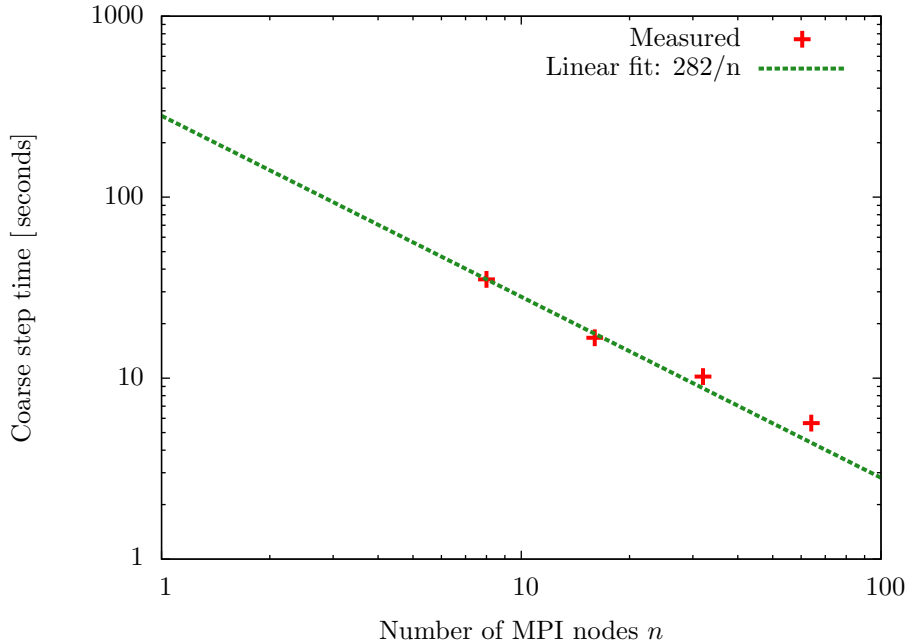
Figure 12: Average time spent in the radiation code (including MPI communication and the radiation substepping) per coarse step for the Test 5 simulation with a fixed 256^3 grid on different numbers of machines.

5.6 Code performance

Since we need to use a cluster of machines for large simulations, it's important that the program performance scales linearly with the number of machines. To check this, we ran several test simulations (see Section 6.1) on a 256^3 grid using different numbers of machines and measured the time spent in various sections of code. These tests were run on the Titane cluster at CEA Saclay.

Fig. 12 and Fig. 13 show the time spent in the RAMSES and radiation code for the tested configurations. They show that both the radiation code and the existing RAMSES code scale linearly with the number of machines.

Fig. 14 shows the time spent in various parts of the code for a 256^3 cosmological simulation (see Section 7.3). The radiation code occupies about 60% of the total coarse step time. About half of the radiation time is used for MPI network communication and the other half is spent in GPU computation.

It may be possible to optimize the code further by overlapping the boundary MPI communication with some of the computation. For example, ATON cooling can be done in parallel with boundary communication because it operates independently on each cell.

5.7 The Future: adaptive mesh refinement

Currently the code only works with a single grid level. Further levels of refinement aren't supported. However, AMR is an important feature and we will need to support it in the future. It would be difficult to use AMR for radiative transfer on the GPU because the GPU is mostly suited for very homogeneous problems. The speedup is not as good if we need many complicated operations and data transfers.

The idea for the future is to enable AMR for hydrodynamics but to solve for radiative transfer only on the coarse grid level. The RAMSES cooling model will have to be used in this case since cooling is needed for the fine cells too. All the refined grid cells within a coarse cell will have to use the photon density from the coarse level.
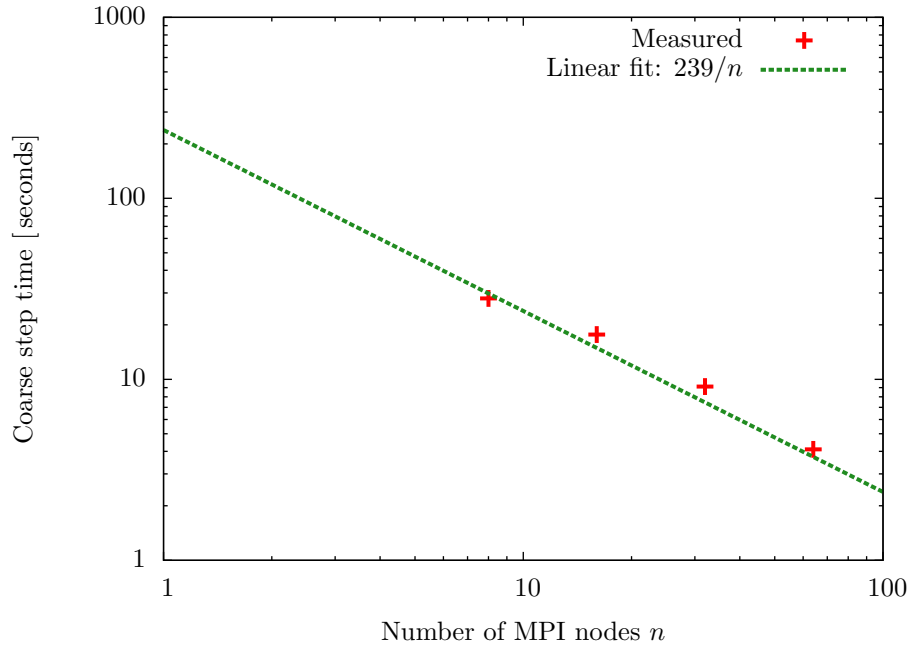
Figure 13: Average time spent in the non-radiation code (including hydrodynamics, RAMSES cooling, star formation) per coarse step for the Test 5 simulation with a fixed 256^3 grid on different numbers of machines.
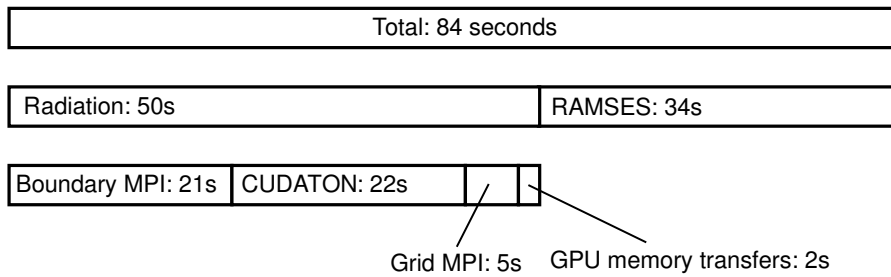

Figure 14: Decomposition of the time spent in various parts of the code for a 256^3 cosmological simulation on 16 MPI nodes.

6 Numerical tests

There are several other codes available that solve hydrodynamics coupled with radiative transfer for astrophysical applications. These codes fall into three main classes: ray tracing codes, Monte Carlo codes and moment-based codes (such as our code). Each of these techniques has its own share of problems and advantages. Illiev et al [13] compared ten radiative transfer codes using three test cases. The results from these codes were mostly in agreement but had some small variations.

In this section, our code is run on two of these test cases and the results are compared to [13]. We have run all the tests using both the RAMSES and ATON cooling models.

6.1 Test 5: Expansion of an ionized bubble

In this test, a single point source of photons turned on in an initially neutral box. The photons ionize the gas to produce an expanding bubble of ionized gas. This is a simplified model of an ionization bubble around a star source during reionization.

The point source of photons is added at the center[1] of the box with emission rate $\dot{N}_\gamma = 5 \times 10^{48}\,\mathrm{s}^{-1}$. The initial conditions of the simulation are as follows:

Total gas number density:	$n_H = 10^{-3}\,\mathrm{cm}^{-3}$
Temperature:	$T = 100\,\mathrm{K}$
Ionized fraction:	$x = 0$
Photon density:	$n_\gamma = 0$
Photon flux:	$F_\gamma = 0$
Box length:	$L = 30\,\mathrm{kpc}$
Grid size:	256^3
Boundary conditions:	zero-gradient
Fixed time step:	$1\,\mathrm{Myr}$.

Snapshots of the state were taken at $t = 10\,\mathrm{Myr}$, $t = 200\,\mathrm{Myr}$ and $t = 500\,\mathrm{Myr}$. To save time, we used a reduced speed of light $\tilde{c} = c/10$. This was shown by [1] to have no significant effect for this type of test. We ran the simulation once using the ATON cooling model and once using the RAMSES model.

6.1.1 Strömgren sphere behaviour

The photons from the source will immediately photoionize the neutral gas ($\gamma + H^0 \to H^+ + e^-$) in the immediate vicinity and heat it up to $\sim 10^4\,\mathrm{K}$ (see Fig. 8). As the source continues to emit more photons, they will move outwards and begin carving out an ionized bubble.

However, the electrons and protons in the bubble also recombine back to neutral hydrogen ($H^+ + e^- \to H^0 + \gamma$). Some source photons will be used up in ionizing the recombined hydrogen again instead of ionizing new atoms at the edge of the bubble. Eventually, the bubble becomes large enough that all the new source photons are used up to reionize the recombined atoms instead of the external netural gas. At this point, the bubble reaches its maximum size and the system is static. This state is called a Strömgren sphere.

The radius of the sphere can be calculated by equating the recombination rate with the source emission rate:

$$\dot{N}_\gamma = V_{\mathrm{ionized}} \alpha_B(T) n_{e^-} n_{H^+}. \tag{68}$$

The Case B recombination rate is used because recombination to the ground state emits another ionizing photon which cancels the effect. Inside the ionized bubble, $n_{e^-} = n_{H^+} = n_H$ and $T \approx 10^4$ K. Therefore the

---

[1]In [13], the source is placed in a corner of the box. However, we have doubled the box length and grid size so the conditions are equivalent.
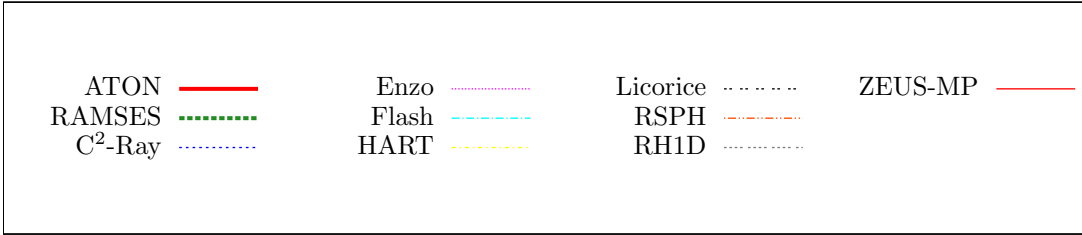
Figure 15: The legend for Test 5 plots.

radius is given by

$$r_s = \left[\frac{3}{4\pi} \frac{\dot{N}_\gamma}{\alpha_B(T) n_{e^-} n_p} \right]^{1/3}. \tag{69}$$

The recombination rate is $\alpha_B(10^4\,\mathrm{K}) = 2.59 \times 10^{-13}\,\mathrm{cm}^3/\mathrm{s}$ which gives

$$r_s = 5.4\,\mathrm{kpc}. \tag{70}$$

This derivation only holds if we ignore hydrodynamics. If the radiation is coupled to hydrodynamics, then the situation is substantially changed. The temperature inside the bubble is $\approx 10^4\,\mathrm{K}$ but the external temperature is $100\,\mathrm{K}$. This creates a large pressure gradient at the boundary which advects the ionized gas further outward until pressure equilibrium is reached. According to [13], the final radius is approximately

$$r_f = \left(\frac{2T_{\mathrm{inside}}}{T_{\mathrm{outside}}} \right)^{2/3} r_s = 184\,\mathrm{kpc}. \tag{71}$$

The box is too small and simulation time too short to see this final state but the point is that the coupling to hydrodynamics has a big effect.

6.1.2   Results

The results from our simulations and those from [13] are shown in Figures 15-19. Since the system is spherically symmetric about the centre of the box, we have plotted the quantities averaged in spherical shells around the centre.

There is a fair amount of variation between all the codes and our results match the other codes reasonably well within this range. Our results most closely match the Enzo code. This because Enzo also uses a moment-based description of radiative transfer on a fixed grid.

The temperature inside the bubble at $t = 10\,\mathrm{Myr}$ (Fig. 17) is lower than expected when using the RAMSES cooling model. However, the correct temperature is reached at later times. This effect is due to the use of chemical equilibrium in the RAMSES model as discussed in Section 3.5. The results for the ATON cooling model are close to the other codes.

The ionized fraction (Fig. 19) drops sharply at the edge of the bubble in our results. This also happens in the Enzo code but other codes have a much weaker cutoff. It is caused by our use of monochromatic photons. As seen in Fig. 3, the photoionization cross section is lower for photons of higher energies. This allows a high energy photon to travel further before undergoing an ionization event. If the code tracks photons in multiple energy groups, each group will travel a slightly different length before ionizing. This smooths out the boundary.
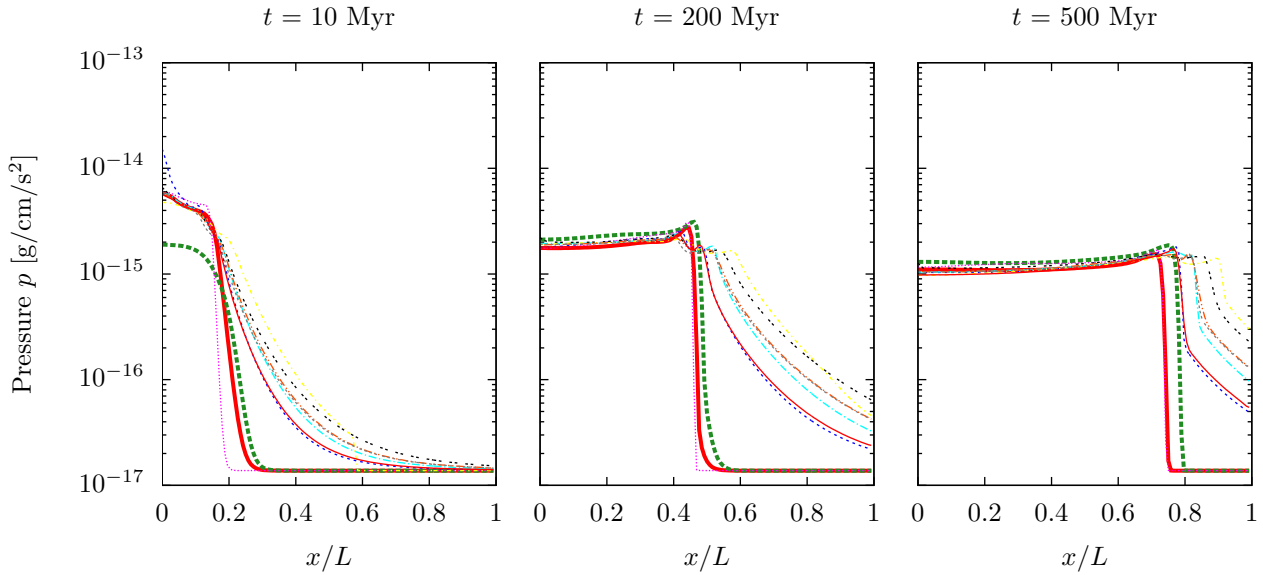
Figure 16: Test 5 results for the pressure p averaged in spherical shells about the box centre. The legend is in Fig. 15.
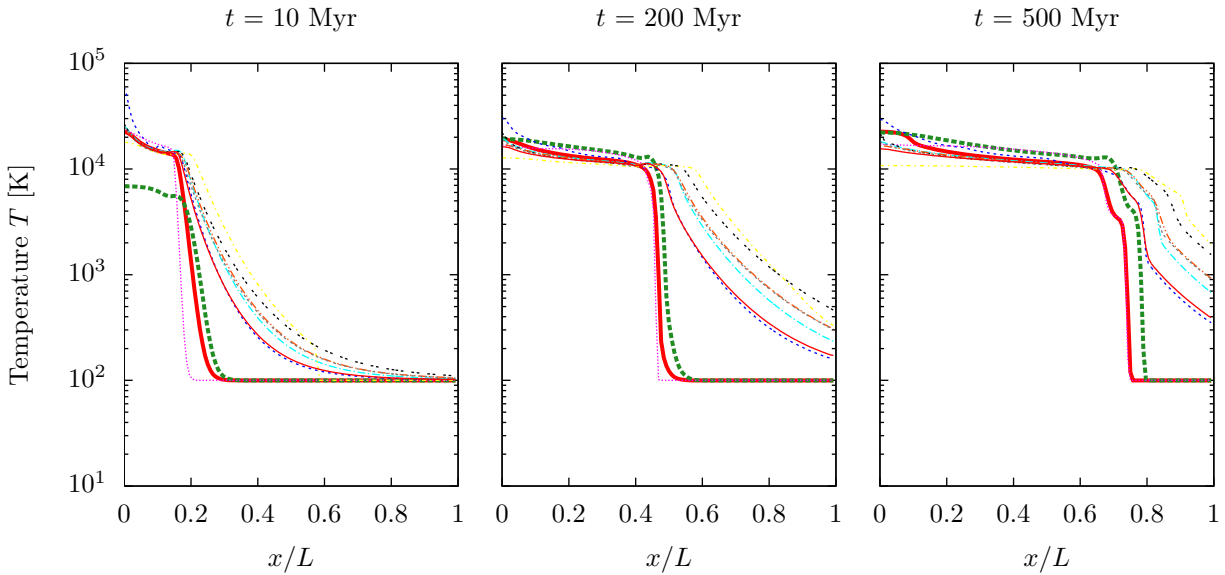

Figure 17: Test 5 results for the temperature T averaged in spherical shells about the box centre. The legend is in Fig. 15. The temperature at $t = 10\,\mathrm{Myr}$ for the RAMSES cooling model is lower than expected due to the chemical equilibrium assumption.
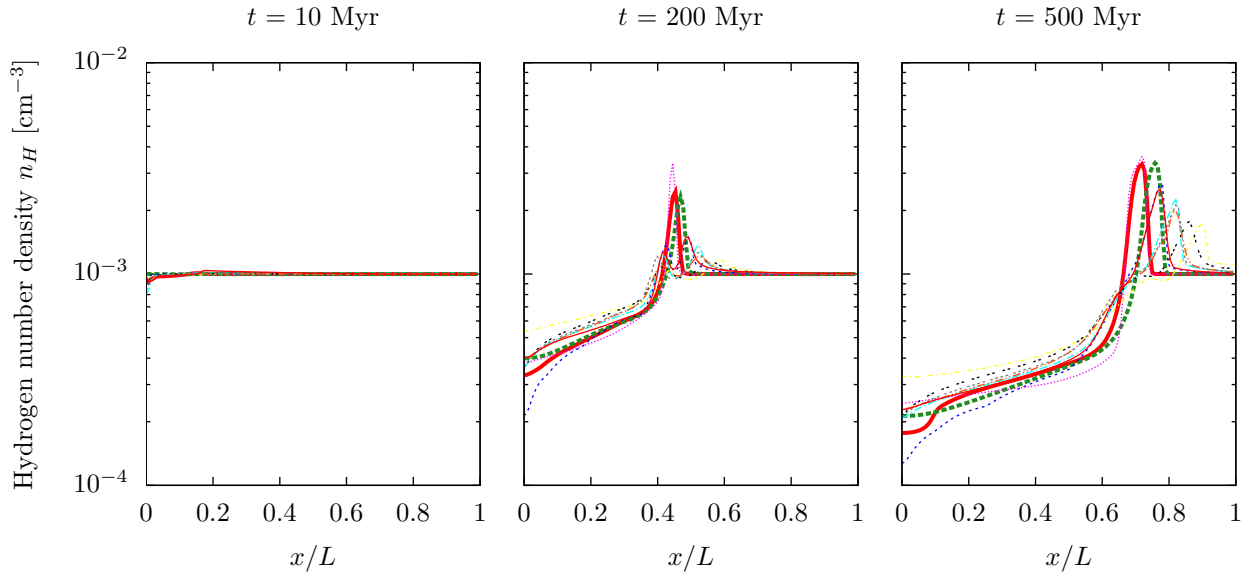
Figure 18: Test 5 results for the gas number density n_H averaged in spherical shells about the box centre. The legend is in Fig. 15.
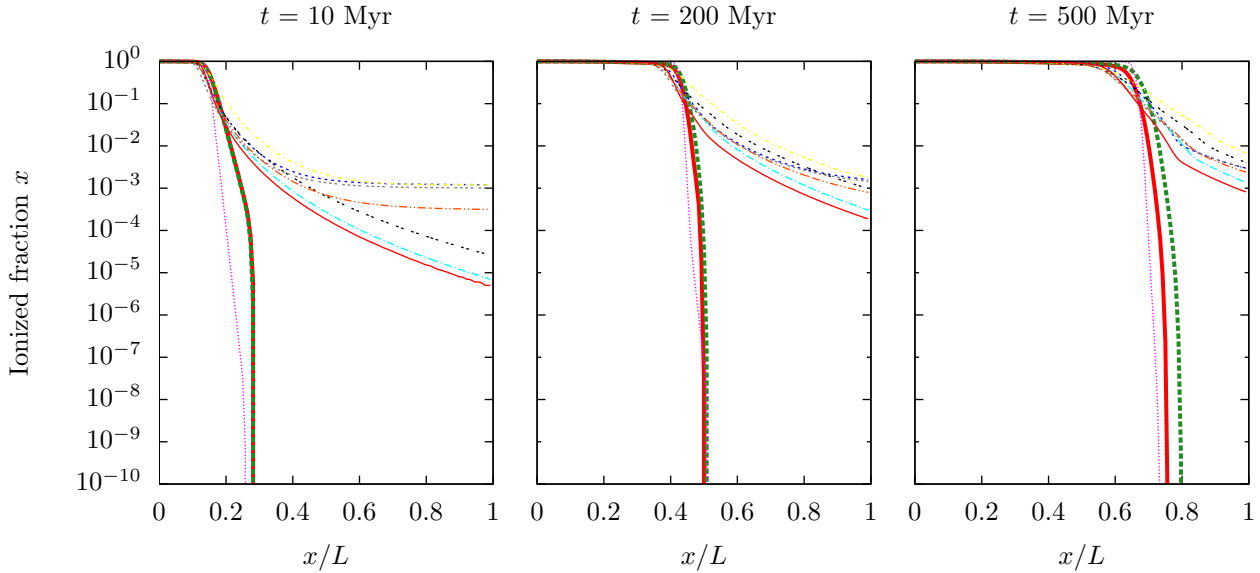

Figure 19: Test 5 results for the ionized fraction x averaged in spherical shells about the box centre. The legend is in Fig. 15. The sharp dropoff at the bubble boundary is caused by our use of monochromatic photons.
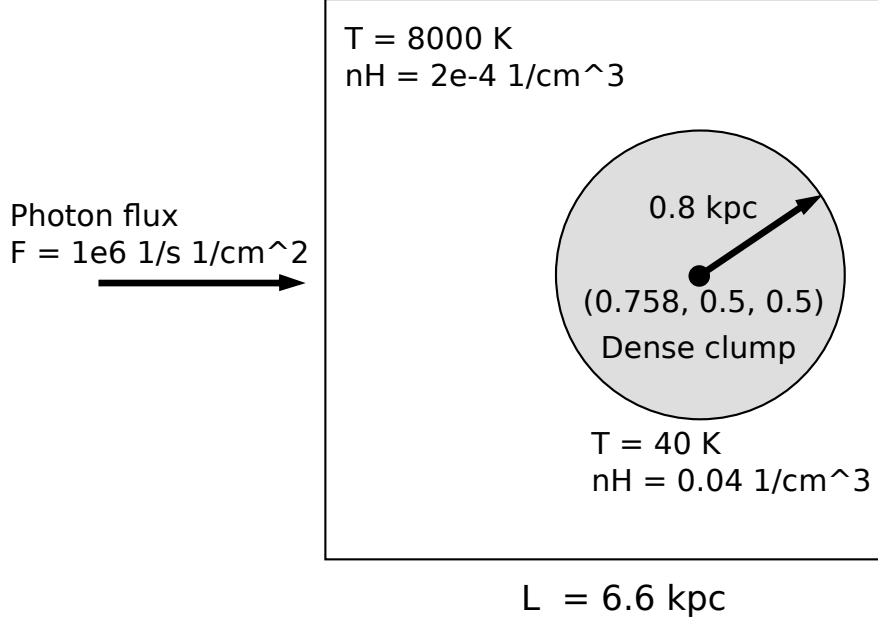
Figure 20: Initial conditions for Test 7.

6.2 Test 7: Photoevaporation of a dense clump

In this test, a wave of photons travels through the box from the left and hits a dense spherical clump of neutral gas on the right (see Fig. 20). The clump is dense enough that the front cannot immediately ionize it. Instead, it is slowly ionized starting from the side facing the incoming wave until the whole clump is eventually consumed.

The clump represents a dense star forming region and the wave front represents radiation from a nearby star. If the radiation heats the clump too much, it will prevent stars from forming there.

The initial conditions of the simulation are as follows:

Box length:	$L = 6.6 \, \text{kpc}$
Grid size:	128^3
Outside gas density:	$n_{H,\text{out}} = 2 \times 10^{-4} \, \text{cm}^{-3}$
Outside temperature:	$T_{\text{out}} = 8 \times 10^3 \, \text{K}$
Clump gas density:	$n_{H,\text{clump}} = 200 \, n_{H,\text{out}} = 4 \times 10^{-2} \, \text{cm}^{-3}$
Clump temperature:	$T_{\text{clump}} = 40 \, \text{K}$
Clump position:	$\mathbf{x}_{\text{clump}} = (0.758, 0.5, 0.5) \times L$
Clump radius:	$r_{\text{clump}} = 0.8 \, \text{kpc}$
Ionized fraction:	$x = 0$
Photon density:	$N_\gamma = 0$
Photon flux:	$F_\gamma = 0$
Boundary conditions:	zero-gradient except on the $x = 0$ boundary
Fixed time step:	$10 \, \text{kyr}$.

A photon flux $\mathbf{F}_\gamma = 10^6 \hat{\mathbf{e}}_1 \, \text{s}^{-1} \, \text{cm}^{-2}$ and and photon density $n_\gamma = |\mathbf{F}_\gamma|/c$ is imposed on the $x = 0$ boundary. Snapshots of the simulation were taken at $t = 1, 5, 10, 25$ and $50 \, \text{Myr}$. The OTSA approximation was used in this test (see Section 3.2.2).

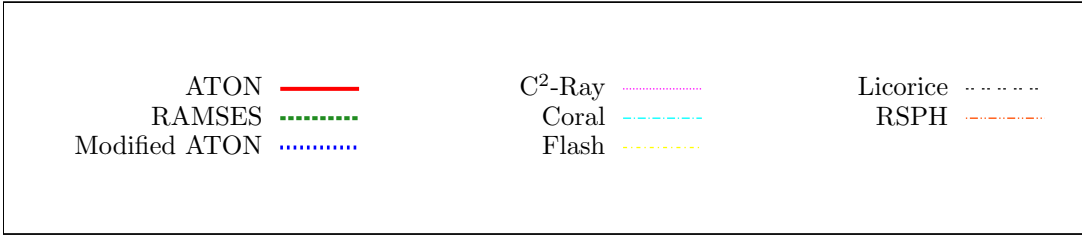| ATON | —— | C^2-Ray | ·········· | Licorice | ·· — ·· — ·· |
| RAMSES | -------- | Coral | — · — · — | RSPH | — · — · — |
| Modified ATON | ············ | Flash | — · — · — |

Figure 21: The legend for Test 7 plots.

6.2.1 Self-shielding

This test demonstrates a radiative transfer effect called **self-shielding**. Ionizing photons are unable to effectively penetrate into very dense neutral regions because they are used up for photoionization. The radiation flux is therefore lower than average in these dense regions and they undergo less heating and ionization as a result. This has important consequences for star formation because stars form where the gas is dense and cold.

6.2.2 Results

The results from our simulations and those from [13] are shown in Figures 21-26. The plots show the quantities along the axis of symmetry through the clump in the direction of the imposed flux.

The major difference between our results and the other codes is the neutral fraction in the region behind the clump in Fig. 25. In the other codes, the clump shields this region from the photons, casting a sharp shadow. The shadow is not as sharp in our results because we use the GLF scheme which introduces too much numerical diffusion. However, this is not really a problem because the sharp shadow is actually unphysical anyway. It was shown in [1] that if OTSA is not used, the isotropic emission of photons from recombination makes the shadow more diffuse. OTSA is an approximation so we should not expect the shadow to be sharp in reality.

Nevertheless, in order to get a better comparison to the other codes, we modified the GLF scheme by taking advantage of the specific conditions of this test. Since the photon flux is strongly directed in the x direction. This means the maximum eigenvalues of the Jacobians for the y and z directions are less than c. We were able to reduce maximum eigenvalues to $0.1c$ without the scheme becoming unstable. This reduced the numerical dispersion in these directions. The results from this modified scheme are labelled "Modified ATON" in the plots. The neutral fraction is much closer to the other codes in this case.

The temperature computed by the RAMSES cooling model is much lower than expected in region to the left of the clump. This is again due to the chemical equilibrium assumption: the gas appears to the model as being initially ionized and therefore isn't rapidly heated by photoionization.

There is also a difference in temperature inside the clump for both the ATON and RAMSES cooling models compared to the other codes. This is caused by the use of monochromatic photons. More energetic photons can penetrate further into the clump and heat it by photoionization.

The gas number density computed using the ATON model is quite close to the other codes.

6.3 Summary

From Test 5 and Test 7, we see that there is still quite a large variation in the results of the available radiative transfer codes. Our results roughly agree with the others.
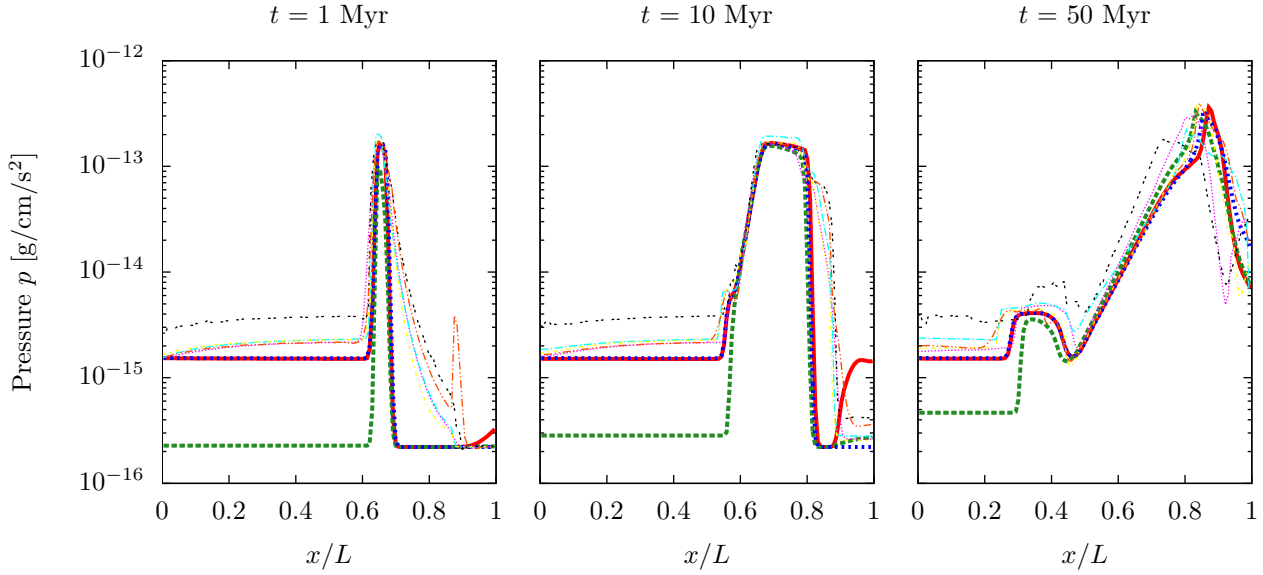
29

Figure 22: Test 7 results for the pressure p along the axis of symmetry through the clump. The legend is in Fig. 21.
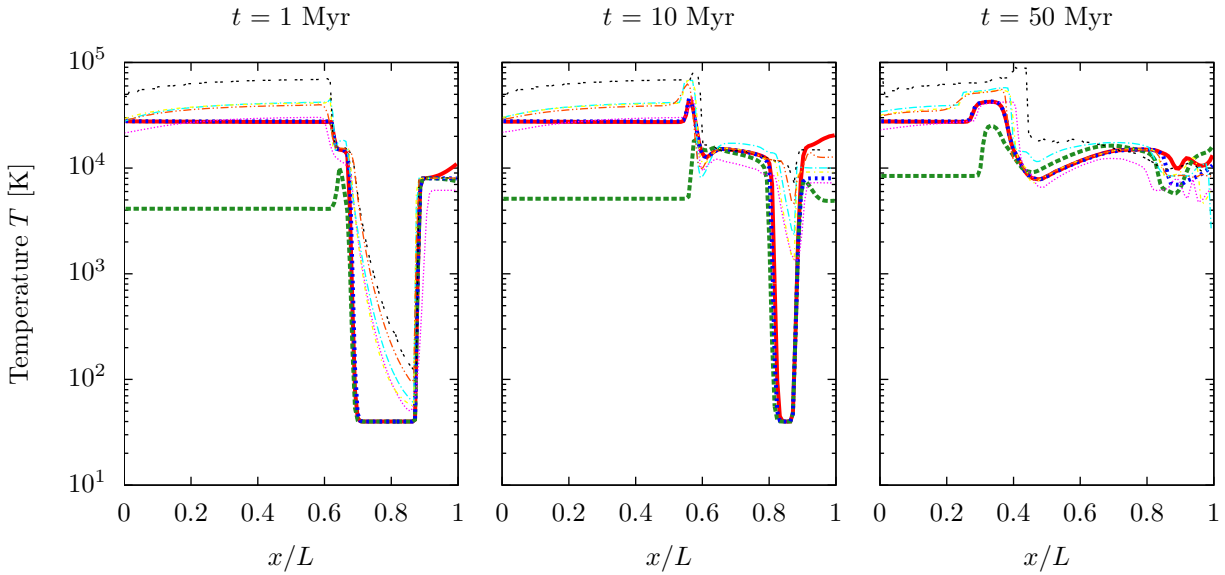

Figure 23: Test 7 results for the temperature T along the axis of symmetry through the clump. The RAMSES temperature is lower than expected due to the chemical equilibrium assumption. Both the ATON and RAMSES temperatures are lower inside the clump due to the use of monochromatic photons. The legend is in Fig. 21.
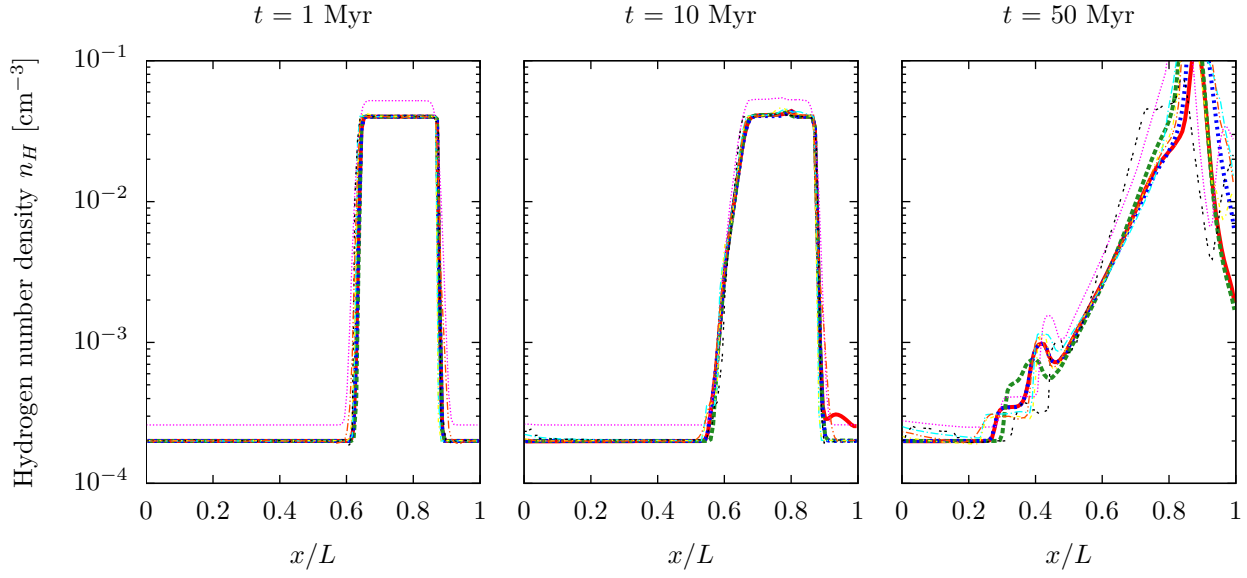
Figure 24: Test 7 results for the gas number density n_H along the axis of symmetry through the clump. The legend is in Fig. 21.
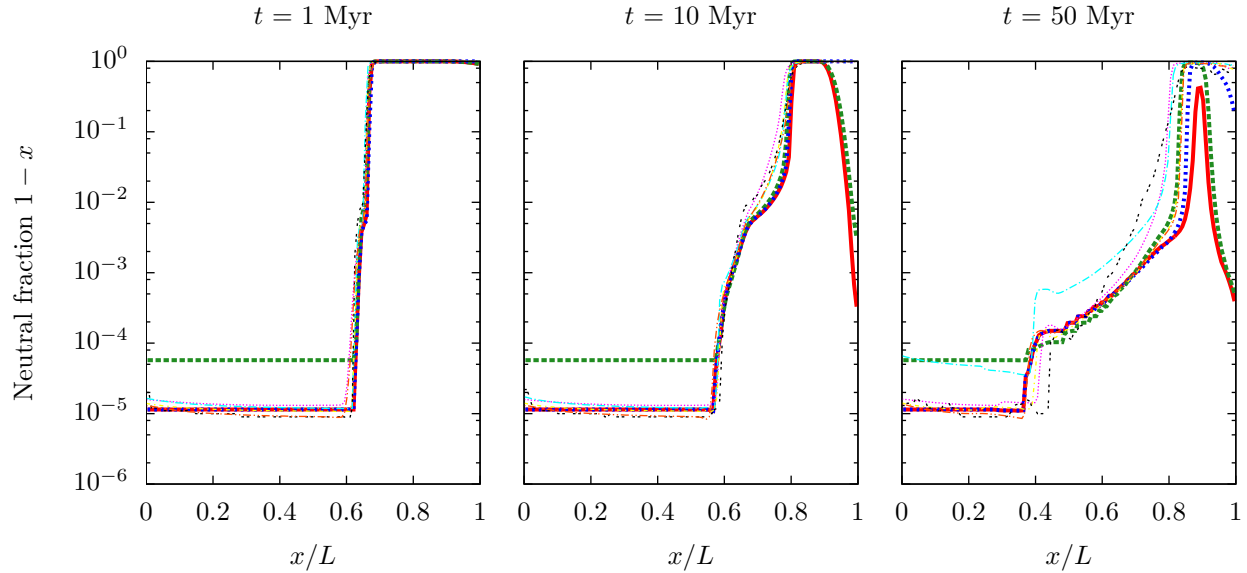

Figure 25: Test 7 results for the neutral fraction $1 - x$ along the axis of symmetry through the clump. The shadow is not as sharp for our results due to numerical diffusion. However, the sharp shadow is not physical anyway. The modified ATON result shows a sharp shadow. The legend is in Fig. 21.
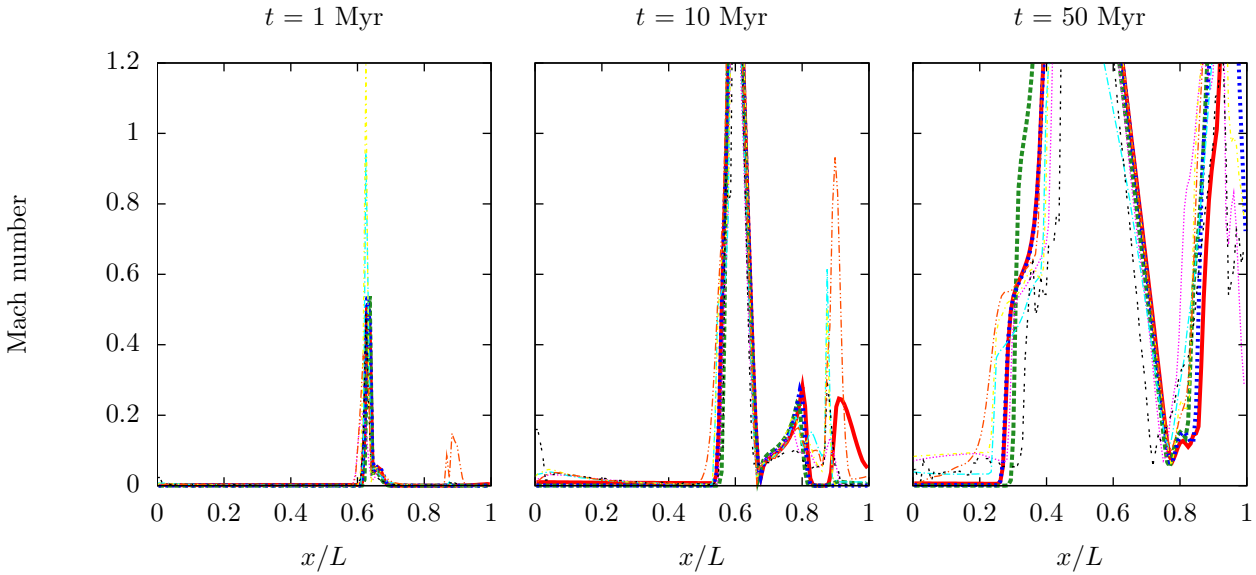
Figure 26: Test 7 results for the Mach number along the axis of symmetry through the clump. The legend is in Fig. 21.

The ATON cooling model is more accurate than the RAMSES model in these tests because the ionized fraction can be quite different to the chemical equilibrium value.

Our use of monochromatic photons causes differences in some cases. This is because the photoionization cross section depends on the photon energy so our photons can only travel a particular distance before undergoing photoionization. Using a spectrum of photon energies would provide a range of distances and smooth out the ionization boundaries.

7   Cosmological simulations

In this section, we apply the radiative transfer code to a cosmological setting with the intention of studying the epoch of reionization. To do this, the hydrodynamical equations need to be modified to take the expansion into account and we need to start the simulation with suitable initial conditions.

7.1   Initial conditions

The initial conditions are created by generating a Gaussian random field and evolving it using linear perturbation theory down to redshift $z = 47$. We used the "`mpgrafic`"[2] program to do this. This program is based on `grafic2` [5]. The cosmological parameters from the WMAP five-year data [15] were used:

Matter density:	$\Omega_m = 0.3$
Dark energy density:	$\Omega_v = 0.7$
Hubble constant:	$H_0 = 70 \, \text{km/s/Mpc}$
Baryon density:	$\Omega_b = 0.04$
Scalar spectral index:	$n_s = 1$ (scale invariant)
Fluctuation amplitude at $8h^{-1}\,\text{Mpc}$:	$\sigma_8 = 0.9$

---

[2]http://www2.iap.fr/users/pichon/mpgrafic.html

7.2 Expansion and supercomoving coordinates

In ΛCDM cosmology, the universe has a flat geometry and expands over time. The distance between two points at rest changes according to

$$x_{\text{physical}}(t) = a(t)x_{\text{comoving}}, \tag{72}$$

where a is called the **scale factor** and x_{comoving} is constant. The derivative of the scale factor is related to the **Hubble parameter** H by

$$H = \frac{1}{a}\frac{da}{dt}. \tag{73}$$

The **redshift** z is defined as

$$z = \frac{1}{a} - 1. \tag{74}$$

As the universe expands, the gas particles move away from each other. Thus the gas density decreases even if the fluid velocity is zero. This violates the the first Euler equation from Eq. 3:

$$\frac{\partial \rho}{\partial t} + \nabla \cdot (\rho \mathbf{u}) = 0. \tag{75}$$

This is because the hydrodynamical conservation equations should be modified in an expanding universe (the covariant derivative of the energy-momentum tensor introduces terms depending on a). For example, first Euler equation becomes

$$\frac{\partial \rho}{\partial t} + \nabla \cdot (\rho \mathbf{u}) + 3H\rho = 0. \tag{76}$$

There is a convenient coordinate transformation that reduces the expanding universe Euler equations to the ordinary equations from Eq. 3. These are the super-comoving coordinates [16]:

$$
\begin{aligned}
d\tilde{t} &= H_0 \frac{dt}{a^2}, \\
\tilde{x} &= \frac{1}{a}\frac{x}{L}, \\
\tilde{\rho} &= a^3 \frac{\rho}{\Omega_m \rho_c}, \\
\tilde{p} &= a^5 \frac{p}{\Omega_m \rho_c H_0^2 L^2}, \\
\tilde{\mathbf{u}} &= a \frac{\mathbf{u}}{H_0 L}, \\
\tilde{n_\gamma} &= a^3 n_\gamma, \\
\tilde{\mathbf{F}_\gamma} &= a^2 \mathbf{F}.
\end{aligned}
\tag{77}
$$

Using these coordinates, Eq. 76 is equivalent to Eq. 75 when all quantities are replaced by the supercomoving versions. So if the velocity is zero, the supercomoving density is conserved even though the proper density is not.

7.3 Results from $12.5\,\text{Mpc}$ box, 256^3 grid simulations

As a first test of the code in a cosmological setting, we used a relatively small grid of only 256^3 cells. Since the grid is small, we also used a small physical box size of length $12.5\,\text{Mpc}$. As for the numerical tests in Section 6, we ran simulations with both the ATON and RAMSES cooling models.

We also ran a third simulation in the "no radiation feedback" mode where the radiation does not affect the hydrodynamics. Instead, the RAMSES cooling model assumes a weak constant background flux and the internal ATON temperature is fixed to a constant value of $10^4\,\text{K}$.

These simulations were run on the Titane cluster at CEA Saclay. Each run used 16 GPUs on 8 machines and took about seven hours to complete.

Since the radiation is sourced by stars, the start of the reionization epoch depends on the star formation rate (SFR). Figure 27 shows the star formation rate obtained from the RAMSES star formation model. The SFR is similar for all three simulations. In larger simulations, it may be possible for the radiation to have an effect on the SFR due to self-shielding.

Figure 28 shows the volume-averaged ionized fraction as a function of redshift. The gas is completely ionized by redshift 4. This is later than the observed end of reionization at $z_{\mathrm{reion}} \approx 6$. However, this is expected because the timing of reionization is strongly dependent on the SFR. The low resolution of the simulation means that highly density peaks are smoothed out and are less likey to form stars which lowers the SFR. The ATON and RAMSES results are very similar.

Figure 29 shows the volume-averaged temperature as a function of redshift. The gas cools adiabatically ($T \propto a^{-2}$) until the beginning of reionization. It is then heated up to 10^4 K by photoionization from the star radiation. The RAMSES temperature increases more slowly than ATON due to the chemical equilibrium assumption.

Figure 30 shows the volume-averaged photon density as a function of redshift. The photon density remains small during reionization because they are absorbed by the ionization events. Once the gas is fully ionized, the photons are no longer absorbed so the density increases quickly.

Figure 31 is a histogram of the neutral fraction distribution of the gas. After reionization, neutral gas remains only in very dense regions.

Figure 32 is a histogram of the temperature distribution of the gas. The low density temperatures are more concentrated around 10^4 K for the ATON model than for RAMSES due to the chemical equilibrium assumption. At high densities, there are two branches in the in the distribution (the lower branch is more distinct). The lower temperature branch is due to self-shielding: photons cannot penetrate into very dense regions and so they aren't heated as much as low density gas. The upper branch is due to photoionization in the immediate vicity of the new stars. They emit so many photons that eventually even the nearby dense region is heated.

Figure 33 is a histogram of the radiation flux and gas density. The flux is quite closely concentrated around $J_{21} = 0.1$ except at high densities where there are again two branches for the same reasons as the high density temperature branches. This is a very clear demonstration of the self-shielding effect discussed in Section 6.2.1.

Figure 34 contains mass-weighted maps of the gas density, star mass density, ionized fraction, temperature and photon flux from just after reionization at $z = 3.3$. Self-shielding can be seen in neutral fraction map as dots of neutral gas at the high density peaks among the overall ionized box.

Figure 34 contains mass-weighted maps from just before reionization at $z = 6.9$. Ionized bubbles can be seen forming and coalescing around the stars. These resemble the Strömgren sphere from Test 5 in Section 6.1.

7.4   Summary

The small $12.5\,\mathrm{M[c}$, 256^3 simulation already captures the qualitative effects of reionization and radiative transfer. In particular, the self-shielding effect is clearly seen in histrograms of the photon flux, netural fraction, temperature, and the neutral fraction map just after reionization. The formation of ionizing bubbles during the reionization process can also be seen.

The next step will be to use the code to run more accurate simulations to study reionization. We are currently preparing a $12.5\,\mathrm{Mpc}$ box, 1024^3 grid simulation using 256 GPUs. The increased resolution will be better for resolving star formation and allow for a more realistic SFR.

8   Conclusions and future applications

By integrating RAMSES and ATON, we have created a code capable of simulating radiative transfer coupled to hydrodynamics. The code agrees with other radiative transfer codes on several test problems and can
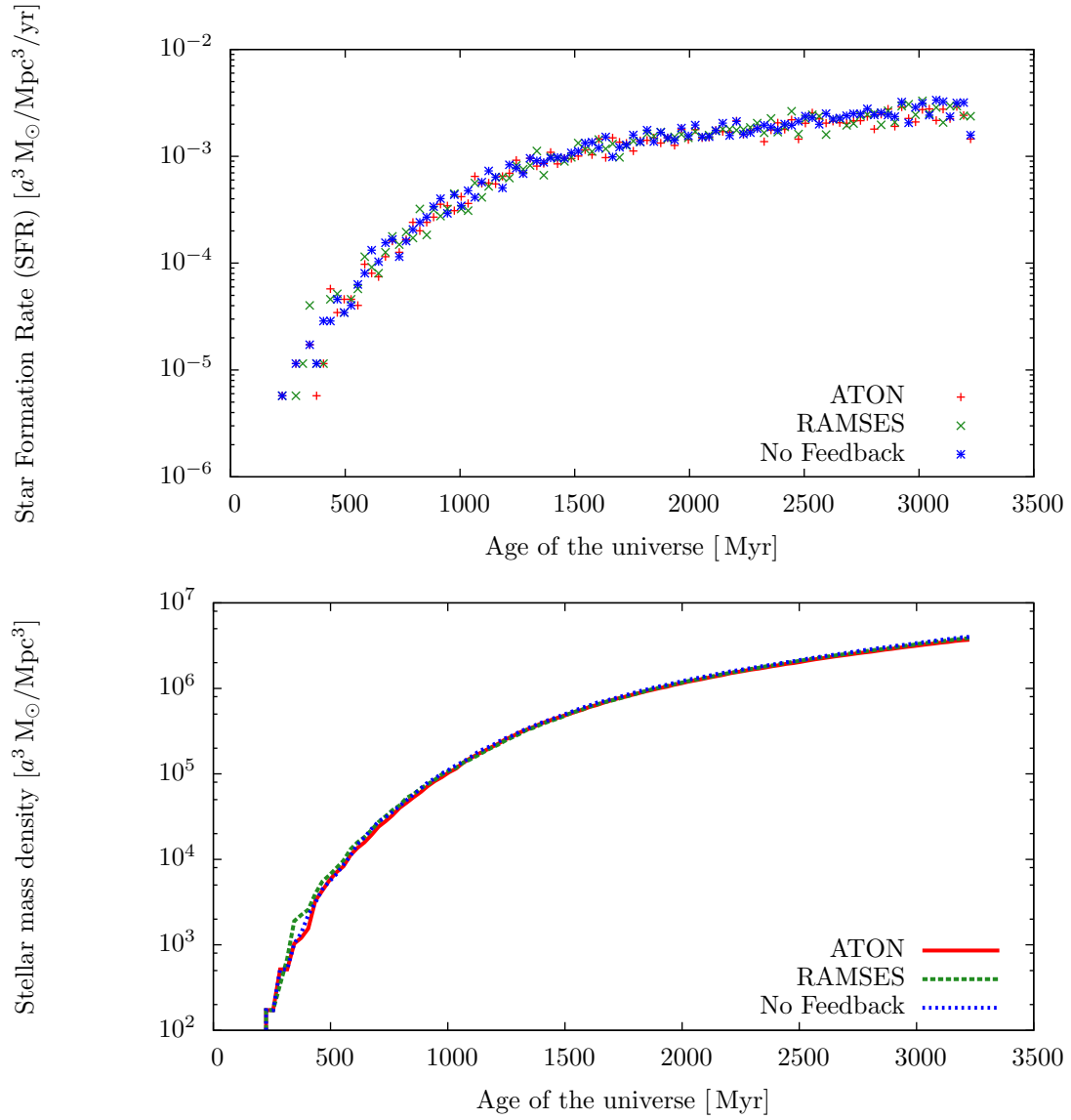
Figure 27: Star formation rate and stellar mass density as a function of the age of the universe for the 12.5 Mpc, 256^3 simulations.
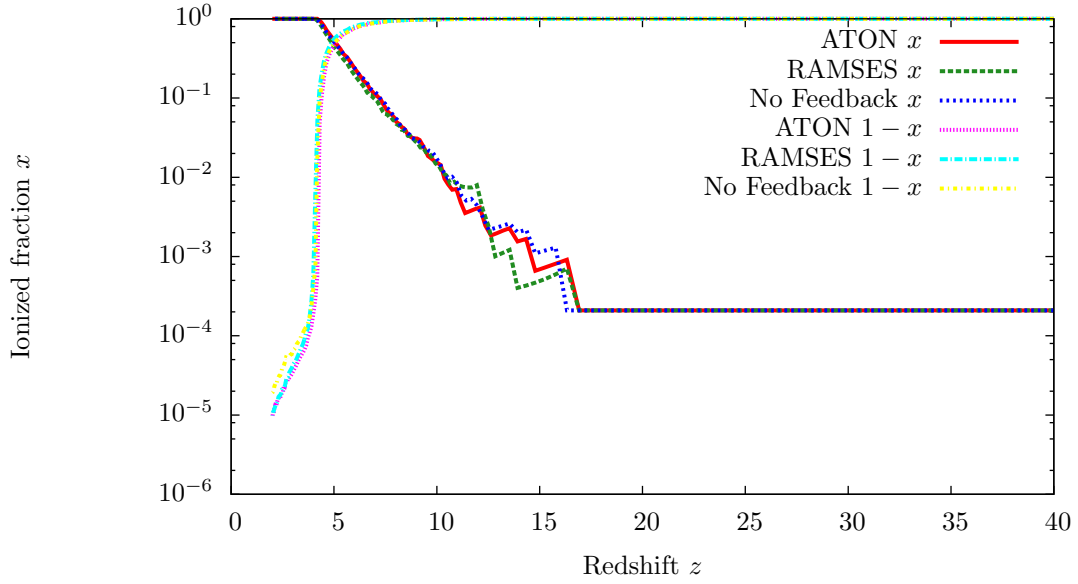
Figure 28: Volume-average ionized fraction as a function of redshift for the $12.5\,\mathrm{Mpc}$, 256^3 simulations.
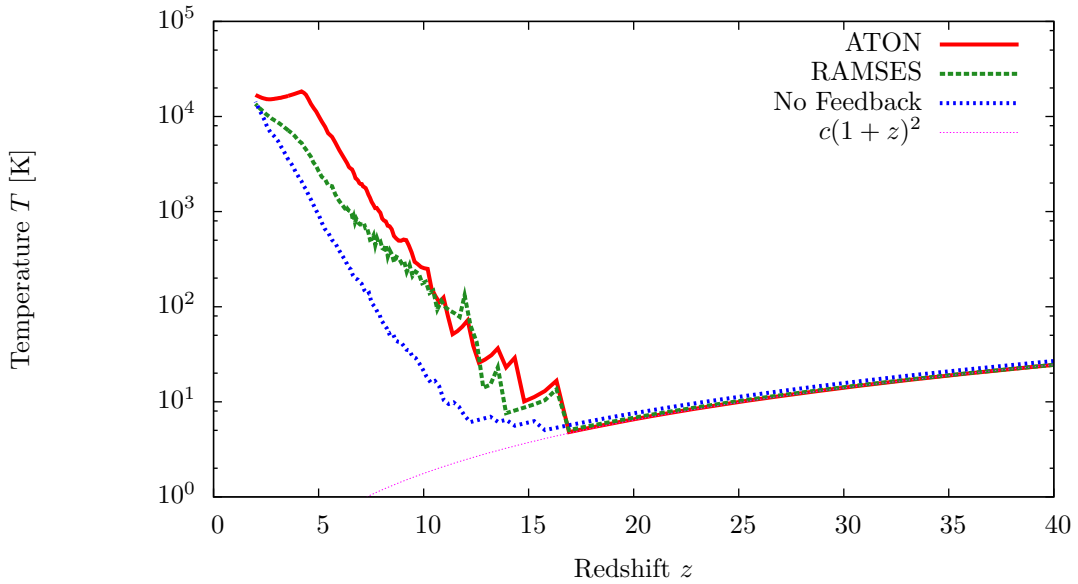

Figure 29: Volume-average temperature as a function of redshift for the $12.5\,\mathrm{Mpc}$, 256^3 simulations.
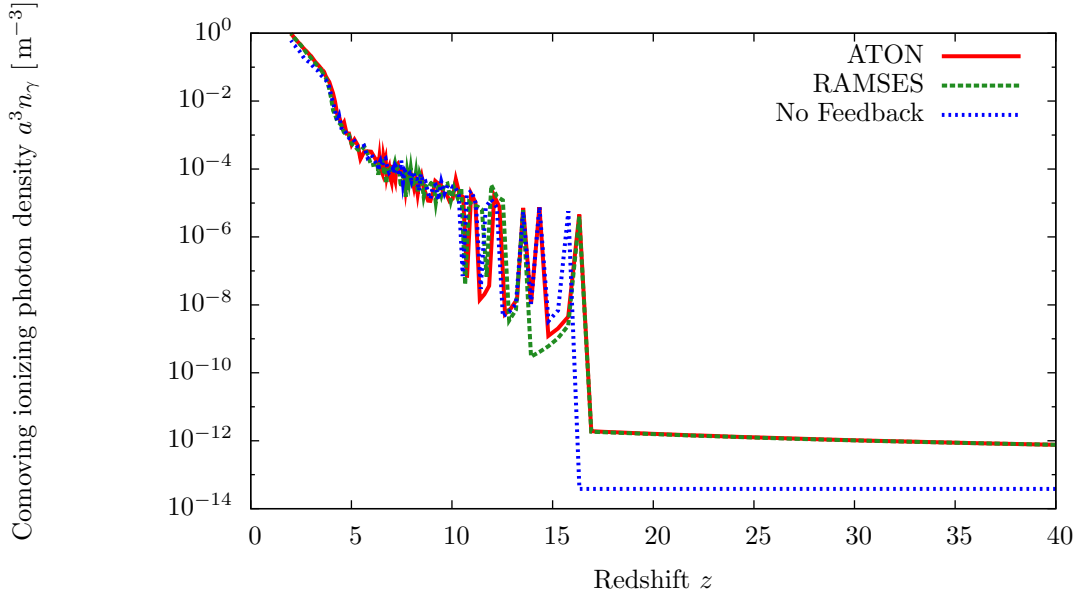
Figure 30: Volume-averaged ionizing photon density as a function of redshift for the $12.5\,\mathrm{Mpc}$, 256^3 simulations.

reproduce the qualitative features of reionization in cosmological simulations. This section describes several applications for these kinds of simulations.

8.1 Lyman-alpha forest

The differencce in energy between the $n = 2$ and $n = 1$ ground state of hydrogen corresponds to a wavelength of 1216 Å. If a photon at this wavelength is incident apon a hydrogen atom, it is readily absorbed by exciting the atom into the $n = 2$ state. The atom will then release another photon to return to the ground state but the photon's outgoing direction is random. Therefore, if we observe the spectrum of a light source through a clump of neutral hydrogen, there will be dip at 1216 Å. This is called the Lyman-α line. Although Lyman-α photons are readily absorbed by neutral hydrogen, they are not affected by ionized hydrogen.

Due to the expansion of the universe, the wavelength of a photon is lengthened as it travels towards us from the source. A photon wavelength λ_0 today corresponds to the Lyman-α wavelength at redshift z where $\lambda_0 = (1 + z)1216$ Å. Thus, the observed spectral intensity at wavelength λ_0 depends on the ionization state at the photon's position at redshift z. By observing the spectrum of a distant light source, we can measure the ionization state along the line-of-sight between us and the source as a function of redshift.

For example, the spectra of high redshift quasars can be used to observe the universe just after reionization. Fig. 36 shows some examples of observed quasar spectra from [8]. The most distant quasar spectra show almost complete absorption for $z \gtrsim 6$. This is a Gunn-Peterson trough and indicates that the was still some neutral hydrogen around at this time. These measurements help to constrains timing of the epoch of reionization.

The distribution of neutral gas is very dependent on radiation as we have seen in the cosmological tests from Section 7.3. Therefore, radiative transfer simulations are needed to simulate it accurately. The BOSS project, part of the Sloan Digital Sky Survey, will obtain Lyman-α forest spectra from 160 thousand quasars at redshifts between 2.2 and 3. This will produce a lot of data about the ionization state of the universe which can be compared with the results of radiative transfer simulations to constrain cosmological parameters.
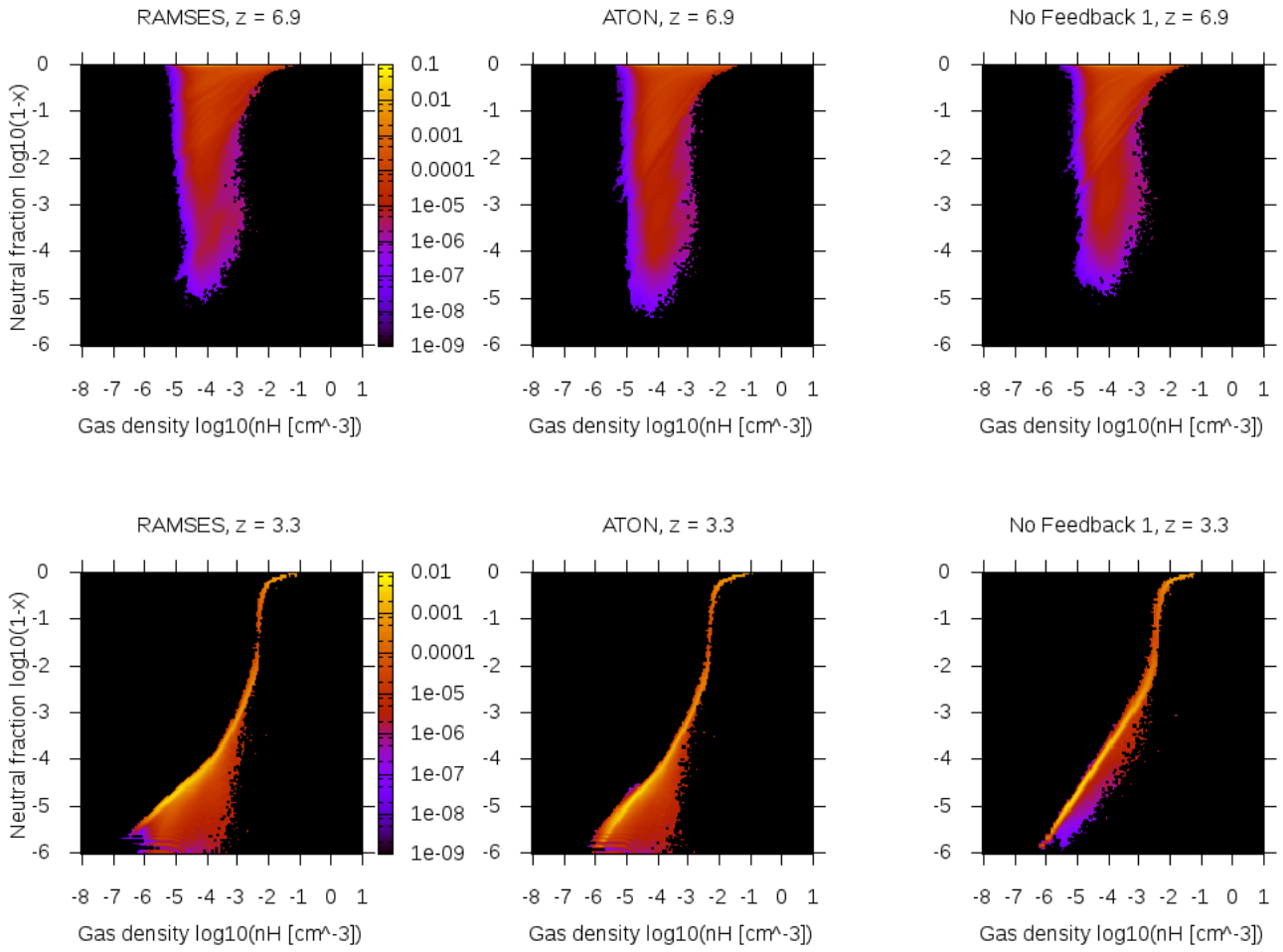
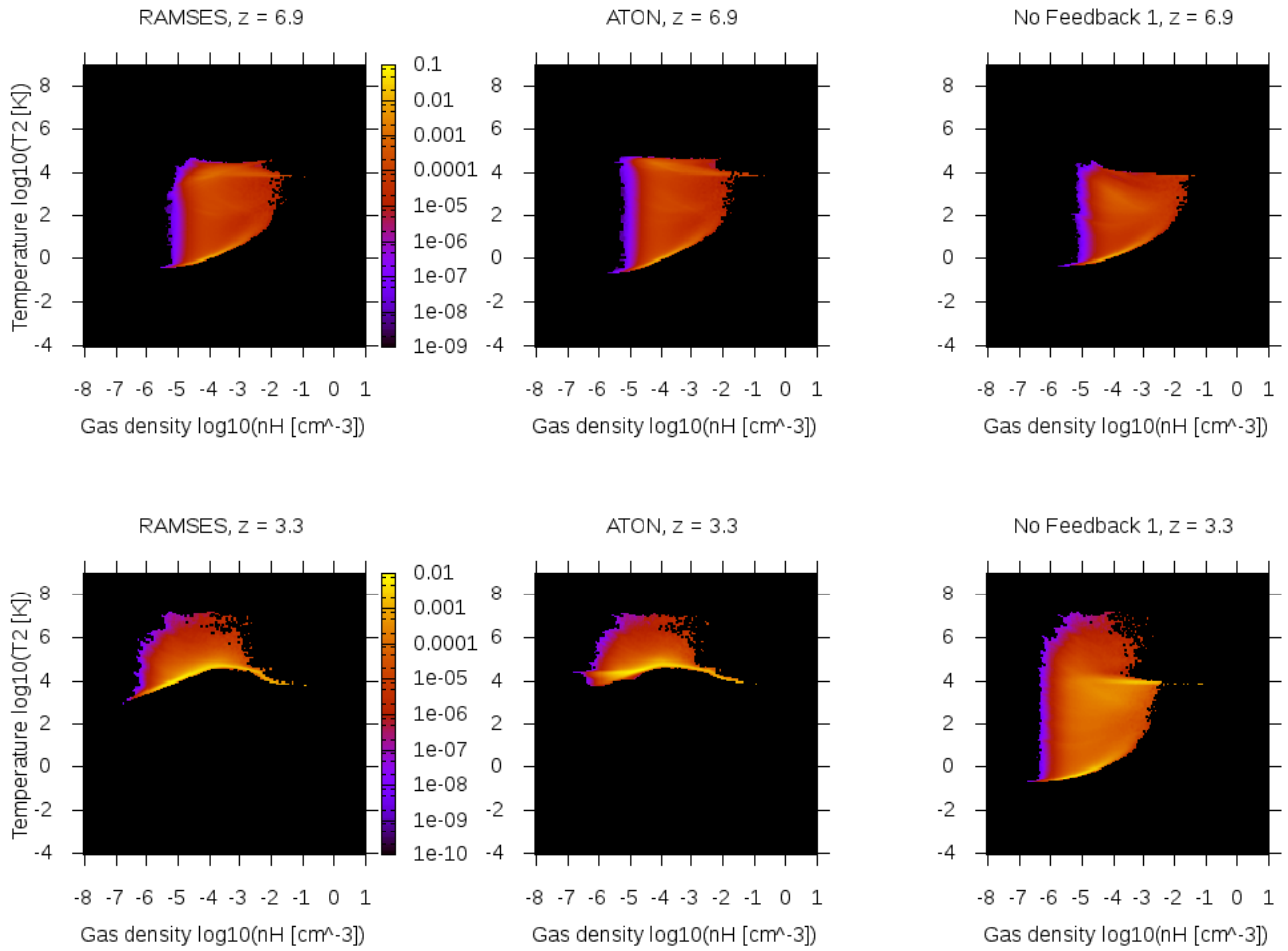Figure 31: Neutral fraction histograms for the 12.5 Mpc, 256^3 simulations.

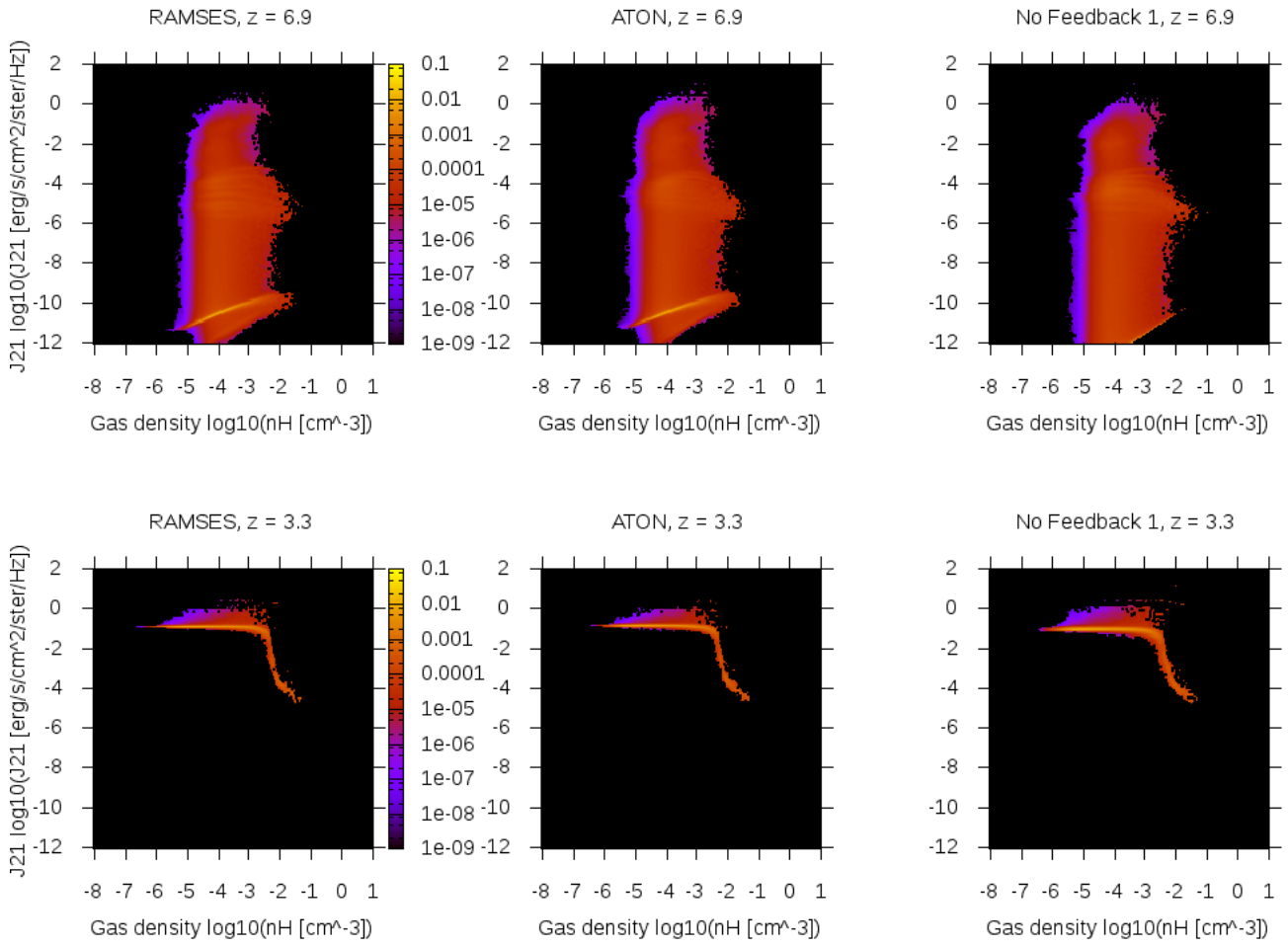Figure 32: Temperature $T_2 = T/\mu$ histograms for the $12.5\,\mathrm{Mpc}$, 256^3 simulations.

Figure 33: Ionizing photon flux J_{21} histograms for the 12.5 Mpc, 256^3 simulations.
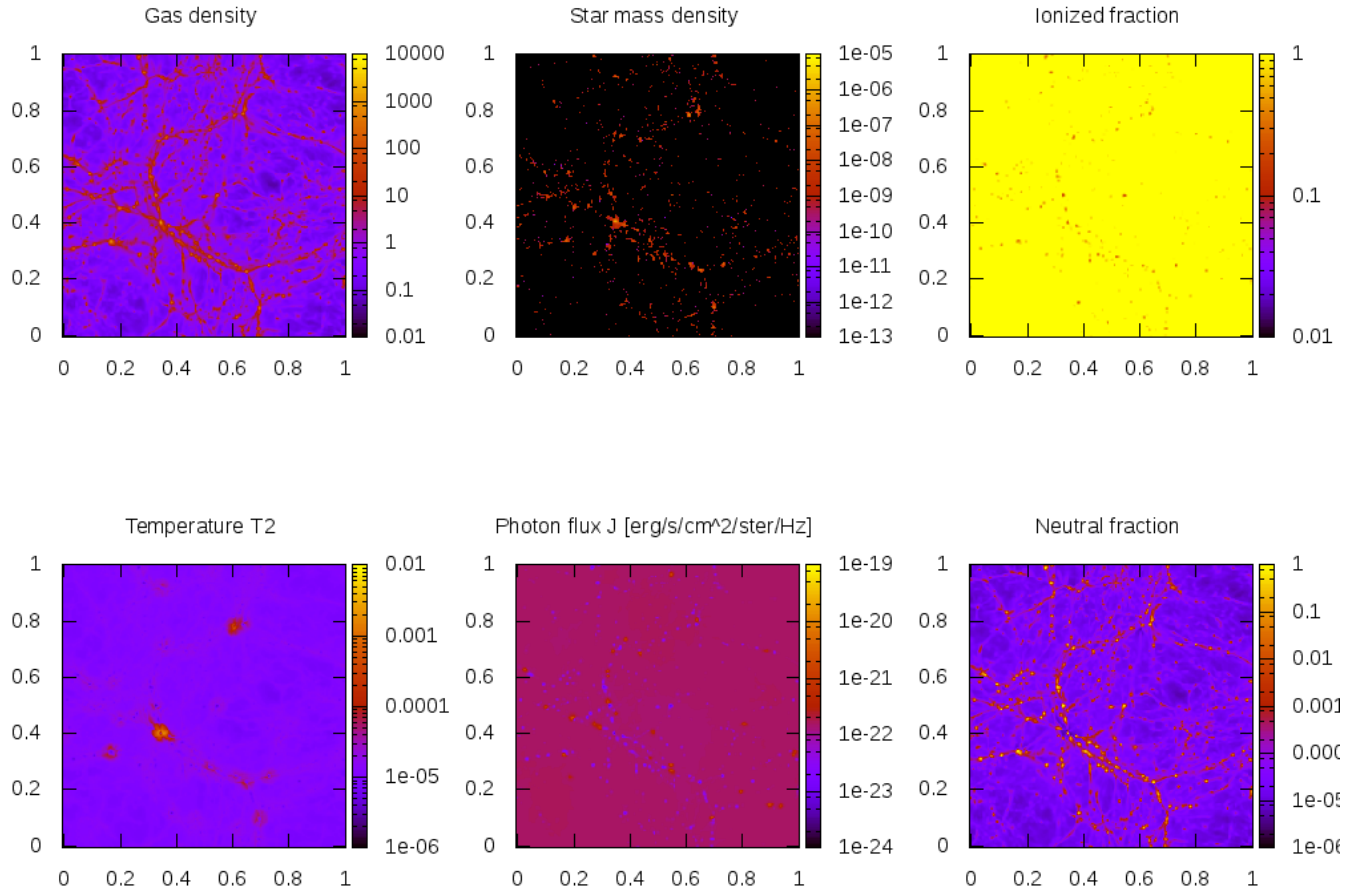
Figure 34: Mass-weighted $z = 3.3$ maps averaged over each z column for the 12.5 Mpc, 256^3 ATON simulation. Dimensionless supercomoving units are used.
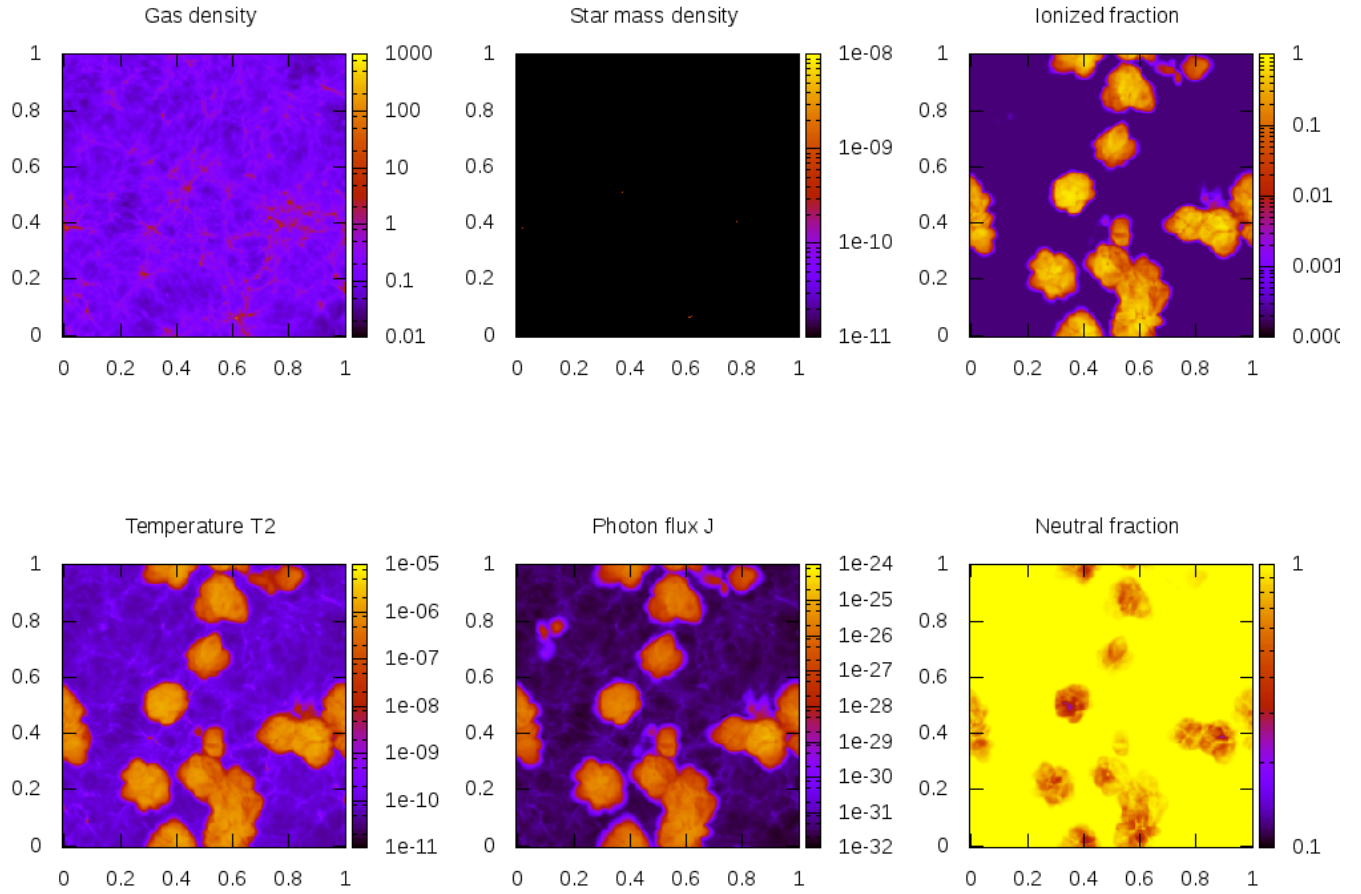
41

Figure 35: Mass-weighted $z = 6.9$ maps averaged over $0.4 < z < 0.6$ for the $12.5\,\mathrm{Mpc}$, 256^3 ATON simulation. Dimensionless supercomoving units are used.
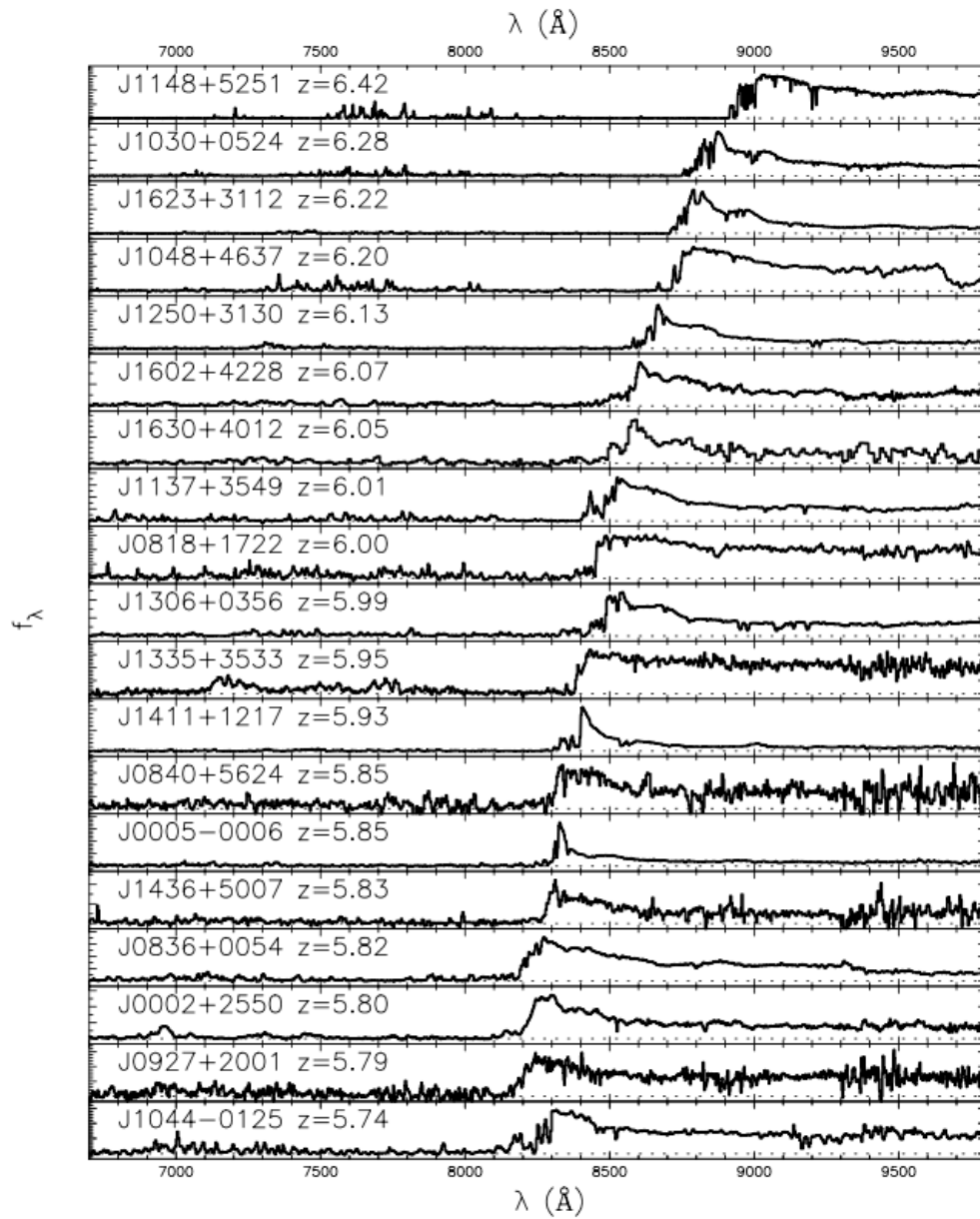
Figure 36: Spectra observed from distant quasars showing Lyman-α absorption. This figure was taken from [8].

8.2 21cm probe of reionization

The ground state of hydrogen is split into two 'hyperfine' levels due to the interaction between the spins of the proton and electron. The energy difference between these levels is very small. It corresponds to a photon wavelength of 21 cm. If some of the neutral hydrogen is in the upper state, it can transition to the lower state by emitting a 21 cm photon.

Since these 21 cm photons are only emitted by neutral hydrogen, they can be used to observe the ionization state as a function of redshift in a similar way to Lyman-α forest. However, the emission can be observed all over the sky, not just from point light sources. In theory, it's possible to use the observations to construct a 3-d map of the neutral hydrogen distribution. These maps can again be compared against radiative transfer simulations.

The 21cm photons will be observed by several radio telescopes including LOFAR, Murchison Widefield Array, 21CMA and the Square Kilometer Array [10].

8.3 Galaxy formation

Besides reionization, a radiative transfer code is also useful for studying galaxy formation [9]. Without radiative transfer, a background radiation field is usually assumed. However, this fails to capture the self-shielding effect discussed in Section 6.2.1. This is important for star formation because stars form where the gas is dense and cold. Also molecular H_2 clouds are sensitive to radiation. Therefore, self-shielding can allow more stars to form. Full radiative transfer simulations are needed to capture this effect in detail.

8.4 Future work

To get more realistic results, we will start running larger simulations with higher resolution. We are currently preparing a 12.5 Mpc box, 1024^3 grid cosmological simulation which is expected to resolve star formation more accurately. For larger box sizes like 100 Mpc, we will need to add support for AMR.

9 Acknowledgments

A User Guide

A.1 Building

The size of the ATON grid is fixed at compile time. The first step is to set it to the desired size in `cudaton/GPU.h`.

Depending on the system, it's usually necessary to set the include and library paths for CUDA in `cudaton/Makefile` and `ramses/bin/Makefile`.

The code can then be built in two parts: First compile the CUDA and C code in the `cudaton` directory. Then compile the Fortran code in `ramses/bin`. The final binary is in `ramses/bin/ramses3d`.

A.2 Namelist parameters

To enable radiation, add `radiation=.true.` in `RUN_PARAMS` section.

There are several parameters for the radiation code. They can be specified in the `RADIATION_PARAMS` section

`radiation_feedback`: true, false
Default: true
If false, the radiation flux will not be returned to RAMSES. So RAMSES will run as if radiation is disabled, but the ionized fraction and photon density will still be evolved independently by ATON. The ATON temperature is fixed at 10^4 K.

`radiation_cooling`: true, false
Default: false
If true, the ATON cooling model is used. If false, the RAMSES model is used.

`rad_boundary_condition`: 0 (zero gradient), 1 (periodic)
Default: 0 (zero-gradient). This may change in the future.

`rad_max_time_step`: double
Default: 0 (meaning infinity)
If nonzero, the coarse time step is clamp to this value or below. It's useful for test cases with uniform initial conditions. The hydrodyanmic time step in these cases is way too large for radiative transfer.

`rad_light_speed_factor`: double
Default: 1.0
The speed of light used for radiative transfer can be reduced by setting a value less than one. This can speed up the simulation but is less accurate.

`allow_gpu_overload`: true, false
Default: false
If more MPI processes are scheduled on a machine than there are GPUs available on the machine, and this is set to false, then the program will print an error message and exit. This is because GPU contention can be slow and such configurations are usually due to operator error.

For Test 5: `rad_num_sources`, `rad_source_[xyz]`, `rad_source_rate`
These parameters can specify a single photon point source.

For Test 7: `rad_flux_at_x_min_boundary`, `rad_flux_[xyz]`, `rad_density`
These parameters are used to impose a flux on the left face of the box.

A.3 Outputs

`output_nnn/radstats`: These are small text files containing averaged physical quantities (the temperature, ionized fraction and photon density) and code timing data.

`output_nnn/radiation`: These are the binary photon density and flux grids. They are used when resuming a simulation.

`output_nnn/hydro`: Besides the normal hydro variables, the AMR output also contains the J_{21} (photon density) field.

A.4 Tools

`ramses/utils/py/rad_history`: Reads the `radstats` files for each output and prints the averaged physical quantities as a function of the redshift.

`ramses/utils/py/star_rate_single`: Reads the output of `utils/f90/getstarlist` and prints out the SFR as a function of the universe age.

`ramses/utils/py/timing`: Averages the radiation timing data for one output.

`ramses/utils/f90/amr2map`: This tool now also supports the J_{21}, x and $1 - x$ quantities.

`ramses/utils/f90/histo`: This tool now also supports the J_{21}, x and $1 - x$ quantities.

References

[1] D. Aubert and R. Teyssier. A radiative transfer scheme for cosmological reionization based on a local Eddington tensor. *Mon. Not. R. Astron. Soc.*, 387:295–307, June 2008.

[2] D. Aubert and R. Teyssier. Reionization Simulations Powered by Graphics Processing Units. I. On the Structure of the Ultraviolet Radiation Field. *Astrophysical Journal*, 724:244–266, November 2010.

[3] S. Baek, P. Di Matteo, B. Semelin, F. Combes, and Y. Revaz. The simulated 21 cm signal during the epoch of reionization: full modeling of the Ly-α pumping. *Astronomy and Astrophysics*, 495:389–405, February 2009.

[4] R. Barkana and A. Loeb. The physics and early history of the intergalactic medium. *Reports on Progress in Physics*, 70:627–657, April 2007.

[5] E. Bertschinger. Multiscale Gaussian Random Fields and Their Application to Cosmological Simulations. *Astrophysical Journal Supplement*, 137:1–20, November 2001.

[6] R. Cen. A hydrodynamic approach to cosmology - Methodology. *Astrophysical Journal Supplement*, 78:341–364, February 1992.

[7] S. Dodelson. *Modern Cosmology*. 2003.

[8] X. Fan, M. A. Strauss, R. H. Becker, R. L. White, J. E. Gunn, G. R. Knapp, G. T. Richards, D. P. Schneider, J. Brinkmann, and M. Fukugita. Constraining the Evolution of the Ionizing Background and the Epoch of Reionization with z~6 Quasars. II. A Sample of 19 Quasars. *Astronomical Journal*, 132:117–136, July 2006.

[9] C. -. Faucher-Giguere, D. Keres, M. Dijkstra, L. Hernquist, and M. Zaldarriaga. Lyman-alpha Cooling Emission from Galaxy Formation. *ArXiv e-prints*, May 2010.

[10] S. R. Furlanetto, A. Lidz, A. Loeb, M. McQuinn, J. R. Pritchard, M. A. Alvarez, D. C. Backer, J. D. Bowman, J. O. Burns, C. L. Carilli, R. Cen, A. Cooray, N. Gnedin, L. J. Greenhill, Z. Haiman, J. N. Hewitt, C. M. Hirata, J. Lazio, A. Mesinger, P. Madau, M. F. Morales, S. P. Oh, J. B. Peterson, Y. M. Pihlström, P. R. Shapiro, M. Tegmark, H. Trac, O. Zahn, and M. Zaldarriaga. Astrophysics from the Highly-Redshifted 21 cm Line. In *astro2010: The Astronomy and Astrophysics Decadal Survey*, volume 2010 of *Astronomy*, pages 83–+, 2009.

[11] Amiram Harten, Peter D. Lax, and Bram van Leer. On upstream differencing and godunov-type schemes for hyperbolic conservation laws. *SIAM Review*, 25(1):35–61, 1983.

[12] L. Hui and N. Y. Gnedin. Equation of state of the photoionized intergalactic medium. *Mon. Not. R. Astron. Soc.*, 292:27–+, November 1997.

[13] I. T. Iliev, D. Whalen, G. Mellema, K. Ahn, S. Baek, N. Y. Gnedin, A. V. Kravtsov, M. Norman, M. Raicevic, D. R. Reynolds, D. Sato, P. R. Shapiro, B. Semelin, J. Smidt, H. Susa, T. Theuns, and M. Umemura. Cosmological radiative transfer comparison project - II. The radiation-hydrodynamic tests. *Mon. Not. R. Astron. Soc.*, 400:1283–1316, December 2009.

[14] N. Katz, D. H. Weinberg, and L. Hernquist. Cosmological Simulations with TreeSPH. *Astrophysical Journal Supplement*, 105:19–+, July 1996.

[15] E. Komatsu, J. Dunkley, M. R. Nolta, C. L. Bennett, B. Gold, G. Hinshaw, N. Jarosik, D. Larson, M. Limon, L. Page, D. N. Spergel, M. Halpern, R. S. Hill, A. Kogut, S. S. Meyer, G. S. Tucker, J. L. Weiland, E. Wollack, and E. L. Wright. Five-Year Wilkinson Microwave Anisotropy Probe Observations: Cosmological Interpretation. *Astrophysical Journal Supplement*, 180:330–376, February 2009.

[16] H. Martel and P. R. Shapiro. A convenient set of comoving cosmological variables and their application. *Mon. Not. R. Astron. Soc.*, 297:467–485, June 1998.

[17] A. Maselli, A. Ferrara, and B. Ciardi. CRASH: a radiative transfer scheme. *Mon. Not. R. Astron. Soc.*, 345:379–394, October 2003.

[18] Andreas Pawlik. *Simulating Cosmic Reionisation*. PhD thesis, Universiteit Leiden, 2009.

[19] R. Teyssier. Cosmological hydrodynamics with adaptive mesh refinement. A new high resolution code called RAMSES. *Astronomy and Astrophysics*, 385:337–364, April 2002.

[20] H. Trac and N. Y. Gnedin. Computer Simulations of Cosmic Reionization. *ArXiv e-prints*, June 2009.

[21] D. A. Verner, G. J. Ferland, K. T. Korista, and D. G. Yakovlev. Atomic Data for Astrophysics. II. New Analytic FITS for Photoionization Cross Sections of Atoms and Ions. *Astrophysical Journal*, 465:487–+, July 1996.